Item 830-H-15 NAS 1.60:1854

JUN 9 1981

NASA Technical Paper 1854

COMPLETED
ORIGINAL

Flight Evaluation of a Simple Total Energy-Rate System With Potential Wind-Shear Application

Aaron J. Ostroff, Richard M. Hueschen,
R. F. Hellbaum, and J. F. Creedon

MAY 1981

NASA

NASA Technical Paper 1854

Flight Evaluation of a Simple Total Energy-Rate System With Potential Wind-Shear Application

Aaron J. Ostroff, Richard M. Hueschen,
R. F. Hellbaum, and J. F. Creedon
Langley Research Center
Hampton, Virginia

National Aeronautics
and Space Administration

**Scientific and Technical
Information Branch**

1981

I

Blank Page

SUMMARY

Wind shears can create havoc during aircraft terminal area operations and have been cited as the primary cause of several major aircraft accidents. A simple sensor, potentially having application to the wind-shear problem, has been developed to rapidly measure aircraft total energy relative to the air mass. Combining this sensor with either a variometer or a rate-of-climb indicator provides a total energy-rate system which has been successfully applied in soaring flight. The measured rate of change of aircraft energy can potentially be used on display/control systems of powered aircraft to reduce glide-slope deviations caused by wind shear.

This paper describes the experimental flight configuration and evaluations of the energy-rate system. Two mathematical models are developed: the first describes operation of the energy probe in a linear design region and the second model is for the nonlinear region. The calculated total energy rate is compared with measured signals for many different flight tests. Time history plots show the two curves to be almost the same for the linear operating region and very close for the nonlinear region.

INTRODUCTION

A simple sensor has been developed to measure aircraft total energy with respect to the air mass. (See refs. 1 to 4.) This sensor consists of a cylindrical tube or probe inserted into the air stream. With a small orifice located on the downstream side of the cylinder, the probe provides a pressure source sensitive to both static and dynamic pressure. The static pressure varies inversely with altitude (and thus potential energy) while the dynamic pressure varies with the square of the velocity (and therefore is proportional to kinetic energy). The sensor pressure coefficient C_p is defined as

$$C_p = \frac{P_{sensor} - P_{static}}{q_c}$$

where q_c is the dynamic pressure and P is the pressure. Probe construction details are contained in reference 2, and the relationship of C_p to physical design trade-offs are given in references 3 and 5. The physical design criteria include probe diameter, orifice size, orifice location along the probe length, and inclination of the probe to the air stream. The probe is used for total energy measurement, and in order to get equal weighting for both the static and dynamic pressures, C_p must equal -1. Data developed in the references include results from wind-tunnel tests which indicate that the desired $C_p = -1$ is achievable with relative insensitivity to sideslip angles. Combining the total

energy-probe pressure source with either a variometer or rate-of-climb indicator provides a total energy-rate system which has been successfully applied in soaring flight. The success of the total energy-rate system in this application and the simple nature of the probe have led to an interest in its applicability to powered aircraft flight to provide information to reduce the effects of wind shear on final approach. Since the system is designed to measure the rate of change of energy with respect to the air mass, the measurement can give a timely indication of wind shear that can be used by display/control system designers in achieving reduced glide-slope deviation caused by wind shear (refs. 6 to 8).

To obtain an understanding of system operation, a limited flight test program was undertaken. The understanding of system performance afforded by flight test data can be used in designing practical display and control systems using this sensor. The flight test results presented in this paper were obtained with the De Havilland DHC-6 Twin Otter aircraft. This aircraft had features which made it well suited as the test vehicle. The physical configuration allowed the total energy probe to be mounted on a boom in front of the aircraft where it was relatively free from body-induced flow-field effects. Instrumentation-wise, the aircraft was equipped with an inertial platform, air data, and body rate sensors, all of which were integrated with a data recording system. The recorded variables made possible an independent calculation of total energy rate which could be compared with the system measurement.

This paper describes the flight test equipment and the sensor configurations evaluated. The maneuvers used to investigate system performance are discussed and the equations used to obtain an independent estimate of aircraft total energy are reviewed. Detailed comparisons of the system output and the independent energy estimates are presented for several flight maneuvers including take-off and landing.

SYMBOLS

A,B	filter transition and control matrices
a,b	first-order break frequencies
C_p	pressure coefficient
C_b^P	matrix transformation from body frame to energy-probe frame
d	lateral distance from center line of vehicle (positive to right)
g	acceleration due to gravity
H	energy height, either potential or kinetic energy
$\dot{H}$	rate of change of energy height
h	vertical distance from center line of vehicle (positive down)
I	identity matrix

k	integer for iteration sample
l	longitudinal distance from vehicle center of gravity (positive forward)
M	Mach number
P	pressure
p	roll rate
q	pitch rate
q_c	dynamic pressure measurement
r	yaw rate
T	temperature
u	control variable
V	velocity
V_{ref}	minimum safe airspeed
X	state variable vector
X_1, X_2	state variables
$X_{1,k}, X_{2,k}$	state variables for kinetic energy
$X_{1,p}, X_{2,p}$	state variables for potential energy
α	angle of attack
β	angle of sideslip
γ	specific-heat ratio of air, 1.4
ΔT	sample time for data reduction
δ	probe sweep angle (forward is negative)
η	recovery factor of total temperature probe, 1.0
θ	measured pitch attitude of vehicle
λ_P	rotation of energy probe about the probe vertical axis
ρ	density

ρ_p rotational angle of probe about vehicle boom

ϕ measured roll angle of vehicle

Subscripts:

bar barometric altitude rate

f filtered

k kinetic energy

kf filtered kinetic energy

m measured

o reference at sea level

P energy probe

PT pitot tube

p potential energy

pf potential energy filtered

s static

t total

X,P longitudinal component at energy probe

X,0 longitudinal component of true value

Y,P lateral component of energy probe

Z,P vertical component of energy probe

α α-vane

β β-vane

0 true value at center of gravity

Notation:

$\{\ \}^b$ vector in body coordinate frame

$\{\ \}^P$ vector in energy-probe coordinate frame

A dot over a symbol indicates differentiation with respect to time.

EXPERIMENTAL CONFIGURATION

The energy probe was evaluated on the Twin Otter aircraft shown in figure 1. This aircraft was being used in an investigation of wind-shear conditions during landing and thus provided an opportunity for cooperative flight test programs. As part of the wind-shear study experimental package, the aircraft was equipped with an instrumentation boom protruding from the nose of the vehicle. The boom, which was instrumented with two total-pressure probes, static-pressure ports, and alpha and beta sensors, provided an energy-probe location with considerably reduced flow-field effects. Figure 2 shows a side view of the energy-probe installation, mounted aft of the alpha and beta vanes. On all the test flights the energy probe was mounted 48° counterclockwise from the vertical looking aft in order to be completely free of boom-induced flow-field effects that could result from pitching motions of the vehicle. Two forward sweep angles δ_p were flown; on one flight the design angle of -20° was used and on three other test flights a δ_p of -34° was flown. The latter case provided data in a nonlinear operating range. A pneumatic filter was used to connect the energy probe with the pressure sensing instrument which was either a variometer or an altitude-rate transducer. The noise filter nominally consists of a cylindrical restrictor, 0.508 mm in diameter and 25.4 mm long, connected in series to a 918 cm^3 tank. This combination provides filtering equivalent to a simple lag circuit, providing a time constant of approximately 2 s. Metallic tubing was used throughout the installation since laboratory tests indicated that the use of soft plastic tubing resulted in significant noise on the signal. Photographs of the instrumentation compartment with the restrictor, filter volume, and tubing are shown in figure 3.

A schematic diagram of the equipment used on most of the test flights is shown in figure 4. Two variometers are shown, one operates on the filtered energy-probe signal and the other operates on the unfiltered energy-probe signal. A differential pressure transducer monitored the pressure differences across the pneumatic filter and a probe monitored the temperature of one of the variometer cases. Two very accurate absolute pressure transducers were added: one monitored the pressure of the filtered energy system and the other monitored static-pressure ports from the boom.

TEST FLIGHTS

The test flights were designed to provide data for the comparison of measured and calculated energy-rate signals and to perform a limited investigation of sensor sensitivity to angles of attack and sideslip and also to attitude rates.

Four distinct test conditions were specified to provide the data of interest. The first required flying the aircraft straight and level at maximum cruise speed for several different altitudes. This test condition provided data for examining the noise levels and linearity of the sensor as a function of altitude. The second test condition was designed to provide data for a change in the aircraft kinetic energy. For this test, the aircraft was stabilized in straight and level flight at maximum cruise speed with the flaps up.

The power was then reduced while the pilot maintained altitude. After the aircraft decelerated to the minimum safe airspeed V_{ref}, full power was applied and the aircraft accelerated back to maximum cruise speed. The third test provided data for a potential/kinetic energy exchange. For this test, the aircraft was first stabilized in a straight and level flight condition at V_{ref}. Without changing power, the pilot pitched the aircraft down to establish a descent rate of 3 m/s. When maximum allowable airspeed was reached (aircraft configuration remained unchanged), the pilot pitched the aircraft up to establish an ascent rate of 3 m/s. The test concluded when the aircraft decelerated to its V_{ref}. The fourth test condition established a potential energy change condition. Again, as in the other conditions, the aircraft was first stabilized in a straight and level condition at V_{ref}. Then the aircraft was pitched down to establish a descent rate of 3 m/s while maintaining the initial airspeed.

An additional flight maneuver was used extensively in the data analysis but was not specified as part of the energy-probe conditions. This condition, called the calibration maneuver, is shown in the results section and consisted of a set of elevator, aileron, and rudder inputs to induce pitch, roll, and yaw cycles, respectively, in the aircraft. These maneuvers helped to magnify the effects of aircraft body rates and sensor location, relative to the aircraft center of gravity, on the energy-rate output.

Table I summarizes the flight test runs that were made to check out the energy probe.

TOTAL ENERGY-RATE CALCULATIONS

This section contains a development of the equations used to model the total energy-rate system. These equations were developed to permit detailed comparison with flight data to verify that the system is a true measure of the change in total energy and to gain a thorough understanding of the individual system components for future wind-shear application studies.

An important parameter that determines probe sensitivity is the coefficient of pressure C_p. Reference 5 presents data describing the change of C_p with forward sweep (probe angle of attack) for several probe configurations. The model developed in this section is for linear range operation of the energy probe in the region where C_p is insensitive to angle of attack. In the appendix, a second model describes the energy-probe performance for larger forward sweep angles where C_p varies nonlinearly with probe angle of attack. Both models use independent vehicle measurements to calculate energy rate. Comparison of the calculated and measured energy-rate time histories for several flights are presented in the following section.

Both linear and nonlinear range models require calculation of both the kinetic and potential energy rates. However, the method of calculation of the kinetic energy rate differs in the two cases. Equations for linear range operation are given in this section; the equations for nonlinear range operation are given in the appendix.

Two methods have been used to calculate true airspeed V_{PT} (ref. 9). The first approach uses measurements of static and dynamic pressure (P_s and q_c) and altitude as follows:

$$V_{PT} = \sqrt{\frac{2\gamma}{(\gamma - 1)} \frac{P_s}{\rho_s} \sqrt{\left(\frac{q_c}{P_s} + 1\right)^{(\gamma-1)/\gamma} - 1}} \tag{1}$$

where γ is the ratio of specific heats for air (1.4) and ρ_s is the static density at flight altitude and is taken from the 1962 standard atmosphere as a function of altitude (ref. 10). The second method incorporates a measurement of total air temperature to calculate true airspeed using equations (2) to (5) as follows (refs. 9 and 11):

$$M = \sqrt{\frac{2}{(\gamma - 1)} \sqrt{\left(\frac{q_c}{P_s} + 1\right)^{(\gamma-1)/\gamma} - 1}} \tag{2}$$

$$T_s = \frac{T_t}{1 + 0.2\eta M^2} \tag{3}$$

$$\rho_s = \frac{T_o}{T_s} \frac{P_s}{P_o} \rho_o \tag{4}$$

$$V_{PT} = M \sqrt{\gamma \frac{P_s}{\rho_s}} \tag{5}$$

where M is the Mach number, T_s is the static temperature at altitude, η is the total-temperature probe recovery factor (1.0) (ref. 11), T_o is the sea-level static air temperature, P_o is the sea-level static pressure, and ρ_o is the sea-level density. The sensors used to measure dynamic pressure, angle of attack, and angle of sideslip are at various locations relative to the vehicle center of gravity, resulting in measurements that are influenced by angular motions of the aircraft. Sensor location is considered in the calculation of the longitudinal velocity at the energy probe $V_{X,P}$ (ref. 12) as

$$V_0 = V_{PT} - (qh_{PT} - rd_{PT}) \tag{6a}$$

$$\alpha_0 = \alpha_m - (pd_\alpha - q\ell_\alpha)/V_0 \tag{6b}$$

$$\beta_0 = \beta_m - (r\ell_\beta - ph_\beta)/V_0 \tag{6c}$$

$$V_{X,0} = V_0 \cos \alpha_0 \cos \beta_0 \tag{6d}$$

$$V_{X,P} = V_{X,0} + (qh_P - rd_P) \tag{6e}$$

In equations (6), p, q, and r represent the vehicle roll, pitch, and yaw rates; ℓ, h, and d represent moment arms from the vehicle center of gravity in the longitudinal, vertical, and lateral directions, respectively; the subscripts 0, PT, α, β, and P refer to the center of gravity, pitot tube, α and β vanes, and the energy probe, respectively; and the subscript m refers to the measured angles. In almost all the test run cases, α_0 and β_0 were less than 10° and generally did not peak simultaneously. Using the small angle approximations, equation (6d) is approximated as

$$V_{X,0} \approx V_0 \tag{7}$$

and equations (6) and (7) combine to become

$$V_{X,P} = V_{PT} + q(h_P - h_{PT}) - r(d_P - d_{PT}) \tag{8}$$

On all Twin Otter flights described in this report, the energy probe and pitot tube were located within 0.3 m of each other on the boom. The correction terms in equation (8) become small in comparison to V_{PT} for small q and r; thus,

$$V_{X,P} \approx V_{PT} \tag{9}$$

On a few test flights, α and β obtained values as high as 15° to 20°. For those cases, the results using equations (6) are slightly better than the results using equation (9). However, the small increase in accuracy did not justify the added complexity. All plots in this paper, for linear range operation, use equation (9). Specific energy, or energy per unit weight, has the units of height and has been referred to in the literature as energy height. (See ref. 6.) In this paper, energy and energy height are used synonymously since the conversion factor is a constant for the flight regime of interest. Equation (9) shows that true airspeed can be used directly in calculating the kinetic energy H_k as

$$H_k = (V_{X,p})^2/2g \tag{10}$$

where g represents the acceleration due to gravity.

The potential energy rate $\dot{H}_{bar}$ is measured by a barometric altimeter in which the electrical signal is differentiated. The pressure sensing device is located along the boom of the vehicle and thus senses pressure changes due to vehicle angular motion. The altitude rate is desired at the energy probe, and thus the measured pitch and roll attitudes (θ and ϕ) are used and the difference in moment arms between the altimeter sensor and energy probe is taken into account to calculate potential energy rate $\dot{H}_p$ as

$$\begin{aligned}\dot{H}_p = \dot{H}_{bar} &- \sin\theta\left[q(h_{bar} - h_p) - r(d_{bar} - d_p)\right] \\ &+ \cos\theta \sin\phi\left[r(l_{bar} - l_p) - p(h_{bar} - h_p)\right] \\ &+ \cos\theta \cos\phi\left[p(d_{bar} - d_p) - q(l_{bar} - l_p)\right]\end{aligned} \tag{11}$$

where the subscript bar refers to the barometric altimeter pressure device.

The energy probe is connected to a restrictor-volume pneumatic filter and a variometer sensor. The pneumatic filter is modeled as a first-order low-pass filter, and both the variometer and the altitude rate transducer are modeled as a combination differentiator and low-pass filter. The differential equation for the combined model is

$$\begin{Bmatrix}\dot{X}_1 \\ \dot{X}_2\end{Bmatrix} = \begin{bmatrix}-b & 1 \\ 0 & -a\end{bmatrix}\begin{Bmatrix}X_1 \\ X_2\end{Bmatrix} + \begin{bmatrix}0 \\ a\ b\end{bmatrix}u \tag{12}$$

where a and b are used to model the low-pass filter break frequency and either the variometer or altitude rate transducer break frequency, X_1 and X_2 are the state variables, and u is the forcing function that represents either the kinetic energy or potential energy rate. Writing equation (12) in more general form

$$\dot{X} = AX + Bu \tag{13}$$

the solution can be obtained directly for discrete sampling intervals ΔT as

$$X(k+1) = e^{A\Delta T}X(k) + A^{-1}\left[e^{A\Delta T} - I\right]Bu(k) \tag{14}$$

where k is an integer representing the iteration sample. For all calculations in this paper, ΔT is 0.2 s, a and b are 0.4 and 1.5 rad/s, respectively. The a and b values were based on laboratory measurements.

The mathematical model of the filtered output variable is different for both the kinetic energy rate and potential energy rate. The kinetic energy H_k (eq. (10)) must be filtered and differentiated and is represented as

$$\dot{H}_{kf} = X_{2,k} - bX_{1,k} \tag{15}$$

whereas the potential energy rate $\dot{H}_p$ (eq. (11)) is only filtered

$$\dot{H}_{pf} = X_{1,p} \tag{16}$$

where the subscripts $1,k$, $2,k$, and $1,p$ refer to equations (12) to (14) which are used for both kinetic energy and potential energy. The total energy rate $\dot{H}$ is

$$\dot{H} = \dot{H}_{kf} + \dot{H}_{pf} \tag{17}$$

RESULTS

This section contains the results from four test flights (table I) and includes time history plots comparing the total energy rate as measured by the energy-rate system with calculated values determined from independent vehicle measurements. Calculated values for both the potential energy rate and kinetic energy rate are also included. On flight 1, the energy probe was mounted at the nominal forward sweep angle δ_p of -20°, which is the case of greatest interest. All these flights are shown for the linear model results. On flights 2 to 4, δ_p was -34°, causing nonlinear operation of the probe. Selected flights illustrating various operations are shown for the nonlinear model results.

Linear Model Results

Figures 5 to 10 contain time history plots for several types of maneuvers, as described in table I for flight 1. These include take-off and landing, calibrations, changes in either kinetic or potential energy, and potential and kinetic energy exchanges. In each figure, the left side contains the three body axis components of vehicle angular rate and the angles of attack and sideslip. Both angles include the corrections due to location on the boom. (See eqs. (6b) and (6c).)

The top plot on the right side is the true airspeed. This signal has been passed through a low-pass filter of approximately 2.5 rad/s, which is high com-

pared to other filter break frequencies in the total energy-probe system. The next plot is for the energy-probe pressure measurement and includes the contribution of the pneumatic filter. This pressure signal is a measure of total energy.

The bottom three plots on the right side relate to the rate of change of energy height; the order of plots is for the potential energy rate, the kinetic energy rate, and the total energy rate. Two curves are shown for the calculated potential energy rate. The solid curve represents the instantaneous change in potential energy rate, whereas the dashed curve shows the effect of filtering. The filtered curve is used in the calculation of total energy rate, since this signal is representative of the potential energy-rate component in the energy-probe measurement. The curve representing the calculated kinetic energy rate is for the filtered signal only. The total energy-rate plots show a comparison between the measured data (solid curve) and the calculated data (dashed curve). The calculated curve results from the summation of the filtered potential and kinetic energy rates shown in the previous plots. In many of the figures, the second page represents a continuation of the run being illustrated. Zero time on the continuation plots represents 70 s into the test run.

Figure 5 is for a take-off with lift-off at approximately 12 s, as illustrated by the $\dot{H}_{pf}$ curve. During take-off, there is an increase in both potential and kinetic energy, causing a large decrease in pressure. At the beginning of any new run, the calculated total energy rate is always initialized to zero, and usually takes approximately 8 s, or 3 filter time constants, to get close to the measured value.

The next four figures (6(a) to 6(d)), are for calibration maneuvers. Figure 6(a) represents a pitch operation, as illustrated in both the q and α_o plots. The effect of system filtering is clearly illustrated in the $\dot{H}_{pf}$ plot. Figures 6(b) and 6(d) are essentially roll maneuvers, whereas figure 6(c) is a yaw/roll maneuver. Figure 6(c) is interesting because the $\dot{H}_{pf}$ curve has a frequency that is twice that of the vehicle yaw/roll frequency. The probable reason for the double frequency is that the vehicle loses lift as it rolls to either side and then regains lift as it returns to the nominal operating point. This high frequency is essentially filtered out, resulting in very little energy change. The pressure measurement is essentially constant for all calibration maneuvers.

Figure 8 represents a kinetic energy change. This is illustrated by first a decrease and then an increase in both V_{PT} and $\dot{H}_{kf}$ curves (fig. 7(a)). For this case, $\dot{H}$ is essentially the same as $\dot{H}_{kf}$. The change in total energy is also illustrated in the plot of pressure P_f. The pressure peaks at close to 40 s, which is approximately the time that the total energy rate passes through zero. The delay in the change in total energy from decreasing to increasing is due to the filtering in the variometer. Figure 7(b) shows V_{PT} leveling off, and $\dot{H}$ converging to zero.

Figure 8 represents an exchange between potential and kinetic energy. As shown in figure 8(a), there is a small increase in kinetic energy for approximately 45 s, accompanied by a much larger decrease in potential energy, resulting in a total energy decrease. In figure 8(b), the potential energy starts

to increase at approximately 25 s (95 s into the run). At the same time, there is a decrease in kinetic energy, which effectively nullifies the potential energy change at the end of the run.

Figure 9 is for a change in potential energy. In figure 9(a), $\dot{H}_{pf}$ shows a decrease in potential energy, whereas an increase in potential energy is shown in figure 9(b).

A landing maneuver is illustrated in figure 10. Most of the total energy change is due to a decrease in potential energy. Touchdown actually occurs at approximately 15 s in figure 10(b). From this time until the end of the run, kinetic energy changes account for the entire decrease in total energy. During the landing run, a large increase is shown in the measured pressure plot, P_f.

Nonlinear Model Results

The intent of this section is to illustrate the modeling results for the nonlinear range (C_p varies nonlinearly with angle of attack) flight tests. A complete description of the nonlinear model is contained in the appendix. Selected runs for flights 2, 3, and 4 are included to verify the modeling approach.

On all three flights, the energy probe was oriented on the vehicle at a sweep angle of -34°, resulting in nonlinear operation of the probe. The only difference between flight 2 and flights 3 and 4 is that the latter two had a variometer and the former an altitude rate device. The energy-rate calculations include the different filter characteristics between the variometer and the altitude rate device.

Results shown for flight 2 include a take-off, three different calibration maneuvers, and a potential/kinetic energy change. In figure 11, the initial plotting time for the take-off run shows the true airspeed V_{pT} to be approximately 15 m/s. Lift-off takes place approximately 10 s later, as shown by the $\dot{H}_{pf}$ trace. Correlation of the measured and calculated total energy-rate curves shows close agreement; however, the calculated energy rate has less dynamic response and slightly less dc gain than the measured energy rate. For the nonlinear model, a trade-off was made between the filter break frequency and dc gain to get the best dynamic response for both low- and high-frequency maneuvers. In general, the results in figure 11 closely resemble those for the take-off run shown in figure 5.

Figure 12 includes results for three different calibration maneuvers. A pitch maneuver, illustrated by the q and α_0 curves, is shown in figure 12(a). Correlation between the measured and calculated total energy-rate curves shows slight variations. Two sources of possible error affecting the calculations are (1) the altitude rate sensor output with peak amplitudes very close to the sensor saturation limits and (2) laboratory tests indicated that the pneumatic filter has a nonlinear transfer function with a decreasing bandpass for increasing input amplitude signals.

Results for the roll maneuvers in figure 12(b) show extremely good correlation for total energy rate. The double frequency effect on $\dot{H}_{pf}$ that was described earlier, is illustrated in this figure and more clearly in the yaw/roll maneuver shown in figure 12(c).

Figure 12(d) is the same run as figure 12(c) but has been included to illustrate features used in the nonlinear model calculations. The five plots show the three velocity components in the probe coordinate frame (eqs. (A11) and (A14)) and the angles of attack and sideslip of the probe (eqs. (A16) and (A17)). The probe angle of attack varies sinusoidally from -16° to -42°; therefore, the calculated pressure coefficient C_p varies from -1.0 to -0.856 (eq. (A18)). Although not shown, the kinetic energy (and thus the total energy) has been adjusted to reflect this nonlinearity.

The final selection from flight 2 is a potential/kinetic energy exchange and is shown in figure 13. Figure 13(a) represents an increase in altitude causing a potential energy increase and a decrease in airspeed causing a kinetic energy decrease. The rate of increase of potential energy is greater than the rate of decrease in kinetic energy, resulting in a net increase in total energy. At approximately 65 s, the total energy starts to decrease because the potential energy is decreasing at a faster rate than the kinetic energy is increasing. Figure 13(b) is a continuation of this run and illustrates similar types of activity. The calculated total energy rate closely resembles the measured data during the entire run.

One run has been selected from each of flights 3 and 4 to illustrate the modeling results. Figure 14 for flight 3 is a 70-s calibration run composed of a large pitch rate of approximately 15 deg/s during the first 20 s, a large roll rate of approximately 30 deg/s during the 20 to 40 s time period, and a combination roll and yaw rate of approximately 20 deg/s and 30 deg/s, respectively, during the final 20 s time period. The frequency of these maneuvers are much higher than those described previously; the frequency of the pitch and roll maneuvers are on the order of 1 to 1.5 rad/s, whereas the frequency of the roll/yaw maneuver is approximately 2 rad/s. The angle of attack has peaks of approximately 10° during the pitch rate maneuver, and the angle of sideslip has peak values of approximately 20° during the roll/yaw maneuver. The probe angle of attack α_p shown in the second column, varies over a wide range causing C_p to vary nonlinearly.

The calculated and measured total energy rates show excellent agreement during the first 50 s of flight. The reason for the amplitude discrepancy during the final maneuver has not been identified but is probably the result of additional unmodeled nonlinearities.

The run selected from flight 4 is a 3° climb at essentially a constant velocity (fig. 15). The potential energy rate varies about a level of approximately 3 m/s. Excellent agreement between the measured and calculated total energy rate can be seen.

CONCLUSIONS

Flight tests and analytical studies have been performed to develop a detailed understanding of the energy-probe operation, to evaluate probe performance, and to develop mathematical models for use in applications studies. The Twin Otter configuration provided an environment relatively free of body-induced flow-field effects and the aircraft contained accurate, accessible instrumentation. These features made the aircraft an ideal test bed for the investigation. Based on flight test data, the following conclusions may be drawn:

1. The mathematical model developed for the energy-probe system provides excellent agreement with flight test data for probe operation in the linear region. Time history plots of the calculated and measured energy rate show the two curves to be almost identical for many different types of aircraft maneuvers.

2. Good agreement between flight test data and model predictions was achieved for operation in the nonlinear region. More complex processing is required and in view of the results obtained in the linear region, operation in the nonlinear region is not recommended.

3. The pneumatic filter provides a simple and effective means for supplementing the inherent filtering of the instrumentation.

4. The probe performance in the linear region has demonstrated its utility to detect changes in total energy. The potential of the sensor for application to wind-shear penetration should be investigated.

Langley Research Center
National Aeronautics and Space Administration
Hampton, VA 23665
April 8, 1981

APPENDIX

EQUATIONS FOR NONLINEAR RANGE MODEL

This appendix presents the detailed equations for modeling the energy probe when the probe has an orientation on the vehicle that results in a nonlinear operating range.

True airspeed, wind axis:

Method 1:

$$V_{PT} = \sqrt{\frac{2\gamma}{\gamma - 1}\frac{P_s}{\rho_s}}\sqrt{\left(\frac{q_c}{P_s} + 1\right)^{(\gamma-1)/\gamma} - 1} \tag{A1}$$

Method 2:

$$M = \sqrt{\frac{2}{\gamma - 1}}\sqrt{\left(\frac{q_c}{P_s} + 1\right)^{(\gamma-1)/\gamma} - 1} \tag{A2}$$

$$T_s = \frac{T_t}{1 + 0.2\eta M^2} \tag{A3}$$

$$\rho_s = \frac{T_o}{T_s}\frac{P_s}{P_o}\rho_o \tag{A4}$$

$$V_{PT} = M\sqrt{\gamma\frac{P_s}{\rho_s}} \tag{A5}$$

The wind coordinate frame has the origin fixed to the vehicle and the longitudinal axis directed along the velocity vector of the vehicle relative to the atmosphere (ref. 13).

APPENDIX

True vehicle airspeed, body coordinate frame:

$$V_0 = V_{PT} - (qh_{PT} - rd_{PT}) \tag{A6}$$

$$\alpha_0 = \alpha_m - (pd_\alpha - q\ell_\alpha)/V_0 \tag{A7}$$

$$\beta_0 = \beta_m - (r\ell_\beta - ph_\beta)/V_0 \tag{A8}$$

$$\{V_0\}^b = \begin{Bmatrix} V_0 \cos\alpha_0 \cos\beta_0 \\ V_0 \sin\beta_0 \\ V_0 \sin\alpha_0 \cos\beta_0 \end{Bmatrix} \tag{A9}$$

Airspeed vector at energy probe, body coordinate frame:

$$\{V_p\}^b = \{V_0\}^b + \begin{bmatrix} 0 & -r & q \\ r & 0 & -p \\ -q & p & 0 \end{bmatrix} \begin{Bmatrix} \ell_p \\ d_p \\ h_p \end{Bmatrix} \tag{A10}$$

Airspeed vector at energy probe, probe coordinate frame:

$$\{V_p\}^p = C_b^p \{V_p\}^b \tag{A11}$$

where

$$C_b^p = \begin{bmatrix} \cos\lambda_p \cos\delta_p & \cos\lambda_p \sin\delta_p \sin\rho_p + \sin\lambda_p \cos\rho_p & -\cos\lambda_p \sin\delta_p \cos\rho_p + \sin\lambda_p \sin\rho_p \\ -\sin\lambda_p \cos\delta_p & -\sin\lambda_p \sin\delta_p \sin\rho_p + \cos\lambda_p \cos\rho_p & \sin\lambda_p \sin\delta_p \cos\rho_p + \cos\lambda_p \sin\rho_p \\ \sin\delta_p & -\cos\delta_p \sin\rho_p & \cos\delta_p \cos\rho_p \end{bmatrix} \tag{A12}$$

C_b^p is the matrix transformation from body frame to probe frame and is a function of the angle of rotation about the boom ρ_p, forward sweep angle of the probe δ_p, and twist angle of the probe λ_p.

APPENDIX

The nominal angles for the three flights corresponding to the nonlinear operating ranges are

$$\rho_P = 48^\circ \qquad \delta_P = -34^\circ \qquad \gamma_P = 0^\circ$$

Definition of the energy-probe axes are as follows:

X-axis: directed through probe hole with positive direction on opposite side of hole

Z-axis: downward along probe length

Y-axis: positive direction chosen to complete right-hand coordinate frame

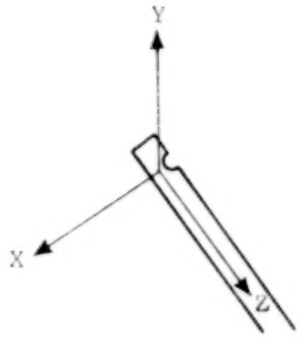

Kinetic energy as measured by energy probe:

$$H_k = (V_{X,P})^2 / 2g \tag{A13}$$

where

$$\{V_P\}^P = \begin{Bmatrix} V_{X,P} \\ V_{Y,P} \\ V_{Z,P} \end{Bmatrix} \tag{A14}$$

The kinetic energy is adjusted by determining a coefficient of pressure C_p which is a function of the energy-probe angles of attack α_p and sideslip β_p. Both α_p and β_p are calculated from components of $\{V_P\}^P$.

Energy-probe angles of attack and sideslip:

$$V_P = \left[(V_{X,P})^2 + (V_{Y,P})^2 + (V_{Z,P})^2 \right]^{1/2} \tag{A15}$$

$$\alpha_p = \tan^{-1} V_{Z,P}/V_{X,P} \tag{A16}$$

$$\beta_p = \sin^{-1} V_{Y,P}/V_P \tag{A17}$$

APPENDIX

Coefficient of pressure:

For $\alpha_p > -0.436$ rad,

$$C_p = -1 \tag{A18a}$$

For $\alpha_p \leq -0.436$ rad,

$$C_p = -1.08176 - 0.0075905\alpha_p + 0.410728(\alpha_p)^2 \tag{A18b}$$

where the coefficients were obtained using a curve fit of data in reference 5.

Adjusted kinetic energy:

$$H_k \leftarrow -C_p H_k \tag{A19}$$

Potential energy rate:

$$\begin{aligned}\dot{H}_p = \dot{H}_{bar} &- \sin\theta \left[q(h_{bar} - h_p) - r(d_{bar} - d_p)\right] \\ &+ \cos\theta \sin\phi \left[r(l_{bar} - l_p) - p(h_{bar} - h_p)\right] \\ &+ \cos\theta \cos\phi \left[p(d_{bar} - d_p) - q(l_{bar} - l_p)\right]\end{aligned} \tag{A20}$$

Solution for filter equations:

$$X(k+1) = e^{A\Delta T} X(k) + A^{-1}\left[e^{A\Delta T} - I\right] Bu(k) \tag{A21}$$

For flights 3 and 4 (altitude-rate transducer),

$$A = -B = -a = -0.5 \text{ rad/s} \tag{A22}$$

Potential energy rate:

$$\dot{H}_p = u \tag{A23a}$$

$$\dot{H}_{pf} = X \tag{A23b}$$

Kinetic energy rate:

$$H_k = u \tag{A24a}$$

$$H_{kf} = a(u - X) \tag{A24b}$$

Flight 2, variometer:

$$A = \begin{bmatrix} -b & 1 \\ 0 & -a \end{bmatrix} = \begin{bmatrix} -0.5 & 1 \\ 0 & -0.4 \end{bmatrix} \tag{A25a}$$

$$B = \begin{bmatrix} 0 \\ a\ b \end{bmatrix} = \begin{bmatrix} 0 \\ 0.2 \end{bmatrix} \tag{A25b}$$

Potential energy rate:

$$X = \begin{Bmatrix} X_{1,p} \\ X_{2,p} \end{Bmatrix} \tag{A26a}$$

$$\dot{H}_p = u \tag{A26b}$$

$$\dot{H}_{pf} = X_{1,p} \tag{A26c}$$

Kinetic energy rate:

$$X = \begin{Bmatrix} X_{1,k} \\ X_{2,k} \end{Bmatrix} \tag{A27a}$$

$$H_k = u \tag{A27b}$$

$$\dot{H}_{kf} = X_{2,k} - bX_{1,k} \tag{A27c}$$

Total energy rate:

$$\dot{H} = \dot{H}_{kf} + \dot{H}_{pf} \tag{A28}$$

REFERENCES

1. Nicks, Oran W.: A Simple Total Energy Sensor. Soaring, vol. 40, no. 9, Sept. 1976, pp. 30-32.

2. Nicks, Oran W.: How To Make a Total Energy Sensor. Soaring, vol. 41, no. 3, Mar. 1977, pp. 23-24.

3. Nicks, Oran W.: A Simple Total Energy Sensor. NASA TM X-73928, 1976.

4. Nicks, Oran W.: Aircraft Total Energy Sensor, U.S. Pat. 4,061,128. Dec. 6, 1977.

5. Nicks, Oran W.: Further Developments in Simple Total Energy Sensors. Science and Technology of Low Speed and Motorless Flight, Perry W. Hanson, compiler, NASA CP-2085, Pt. I, 1979, pp. 219-245.

6. Joppa, Robert G.: Wind Shear Detection Using Measurement of Aircraft Total Energy Change. NASA CR-137839, 1976.

7. Rek, Bron: Windshear Indication Systems. Flight Int., vol. 116, Sept. 22, 1979, pp. 984-986.

8. Greene, R. A.: The Effects of Low-Level Wind Shear on the Approach and Go-Around Performance of a Landing Jet Aircraft. [Preprint] 790568, Soc. Automot. Eng., Apr. 1979.

9. Dommasch, Daniel O.; Sherby, Sydney S.; and Connolly, Thomas F.: Airplane Aerodynamics, Fourth ed. Pitman Pub. Corp., 1967.

10. U.S. Standard Atmosphere, 1962. NASA, U.S. Air Force, and U.S. Weather Bur., Dec. 1962.

11. Kayton, Myron; and Fried, Walter R., eds.: Avionics Navigation Systems, John Wiley & Sons, Inc., c.1969.

12. Gainer, Thomas G.; and Hoffman, Sherwood: Summary of Transformation Equations and Equations of Motion Used in Free-Flight and Wind-Tunnel Data Reduction and Analysis. NASA SP-3070, 1972.

13. Etkin, Bernard: Dynamics of Atmospheric Flight. John Wiley & Sons, Inc., c.1972.

TABLE I.- SUMMARY OF TEST RUNS FOR ENERGY PROBE ON TWIN OTTER FLIGHTS

Flight	Run (a)	Type of run
1	1*	Take-off
1	2*	Calibration maneuver
1	3*	Kinetic energy change
1	4*	Potential/kinetic energy exchange
1	5*	Potential energy change
1	6*	Calibration maneuver
1	7*	Landing
2	1*	Take-off
2	2	Constant altitude (James River Bridge run)
2	3*	Calibration maneuver
2	4	Kinetic energy change
2	5*	Potential/kinetic energy exchange
2	6	Constant altitude h = 914 m
2	7	Constant altitude h = 457 m
3	1	Take-off
3	2	Overflight Thimble Shoals Lighthouse
3	3	Kinetic energy change
3	4	Potential/kinetic energy exchange
3	5*	Calibration maneuvers
3	6	Landing
4	1	Take-off
4	2	Level flight h = 457 m } Energy-probe runs
4	3	Level flight h = 1066 m } Energy-probe runs
4	4	Level flight h = 1676 m } Energy-probe runs
4	5 to 11	Constant altitude = Radar calibration data
4	12 and 13	Track 3^{o} glide slope
4	14*	3^{o} climb
4	15 to 21	Constant altitude data

[a]The results of the runs with an asterisk are the ones given in this report.

BLANK

PAGE

LANGLEY RESEARCH CENTER

Figure 1.- Twin Otter aircraft.

L-73-6350

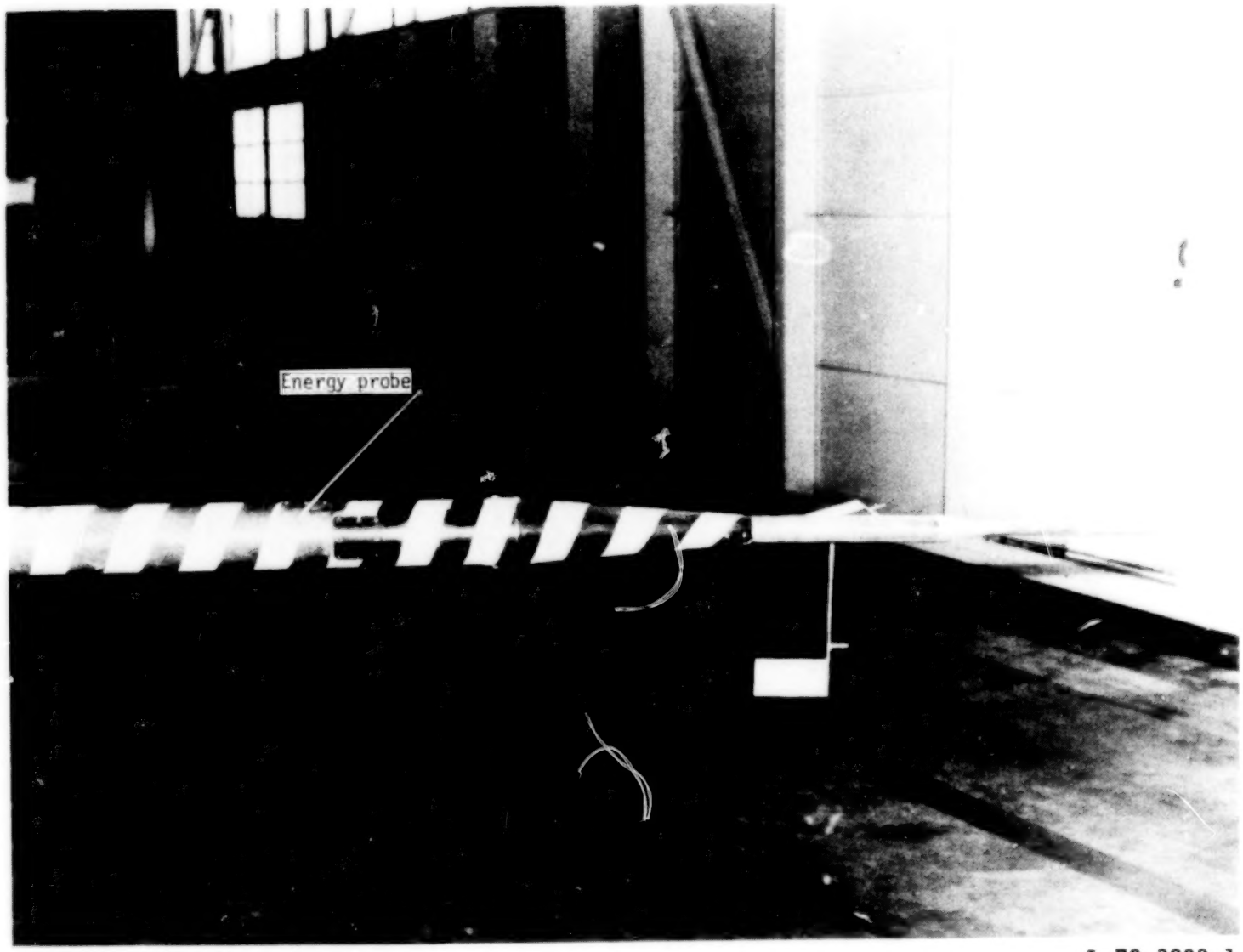

L-79-3892.1

Figure 2.- Side view of energy-probe installation.

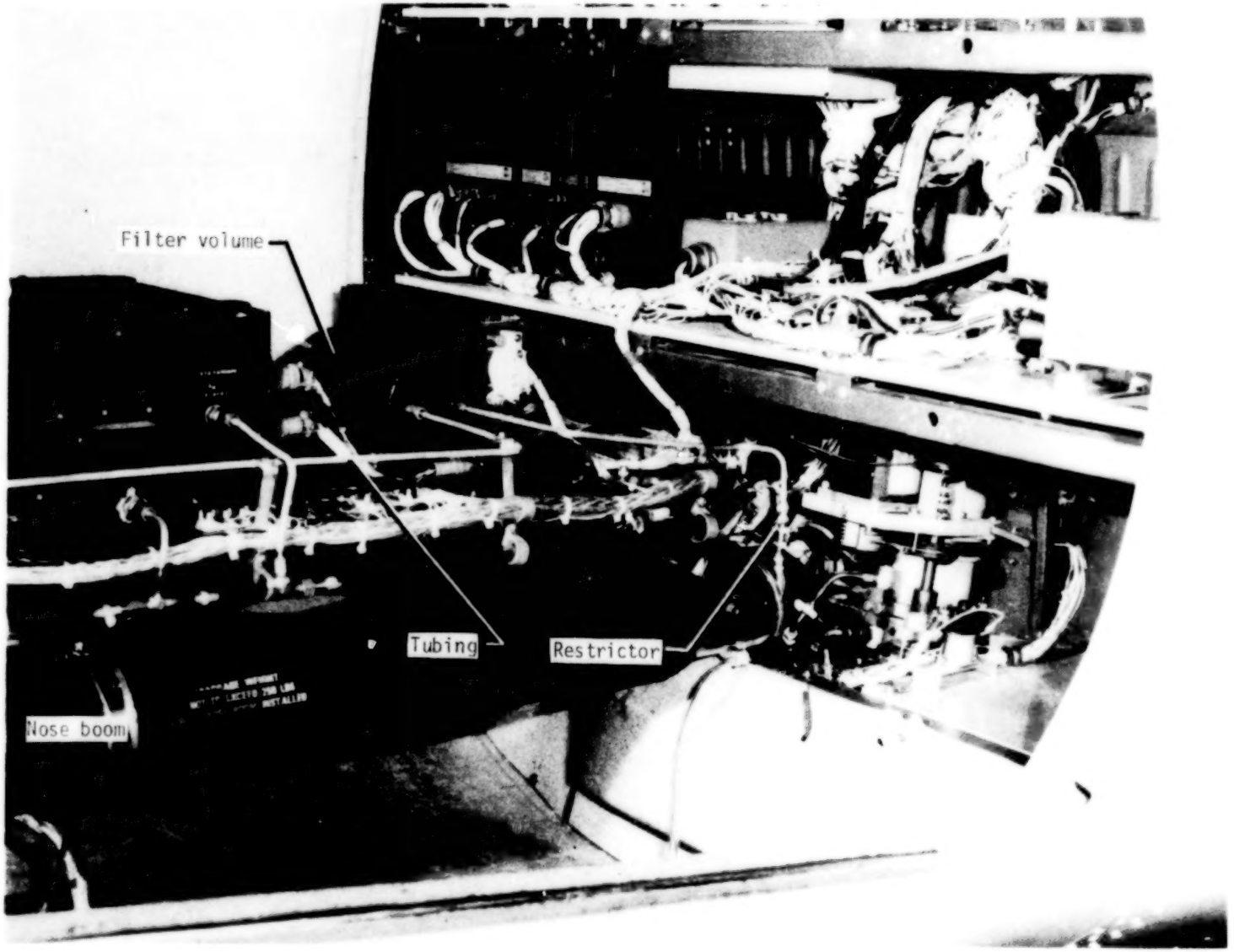

L-79-3889.1

(a) Aft view.

Figure 3.- Instrumentation compartment.

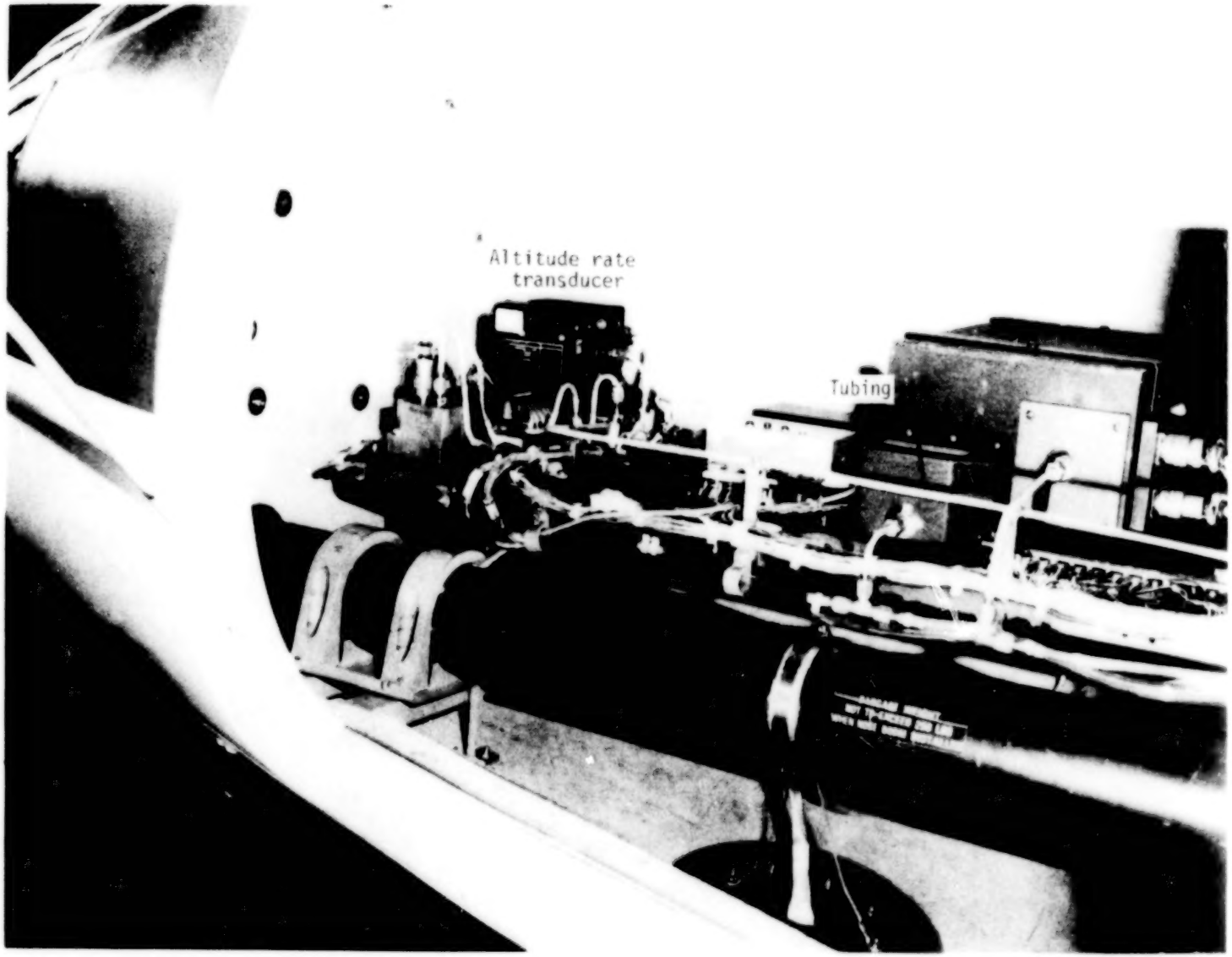

L-79-3890.1

(b) Forward view.

Figure 3.- Concluded.

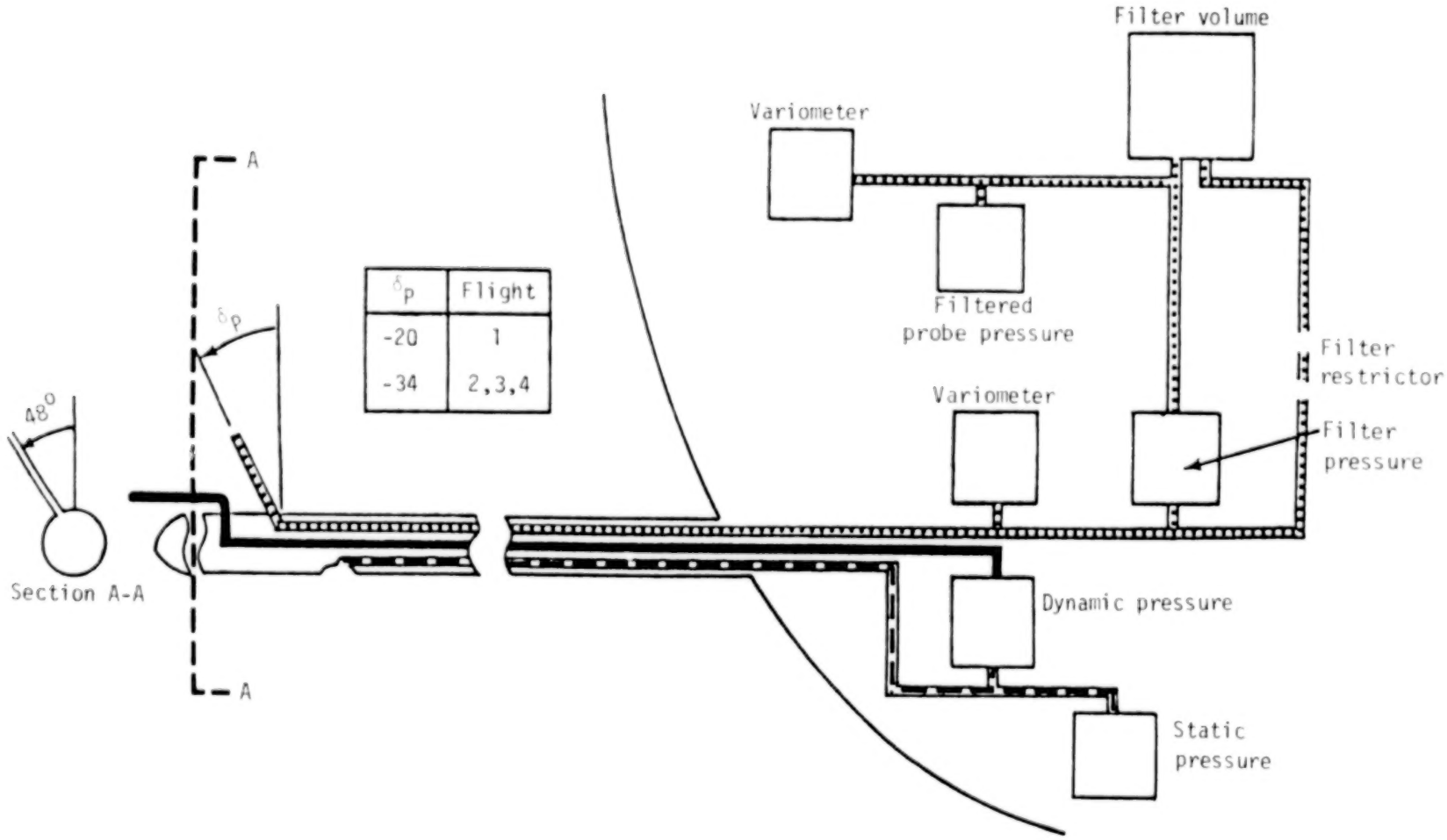

Figure 4.- Schematic diagram for flights 1 and 2 of total energy-rate system.

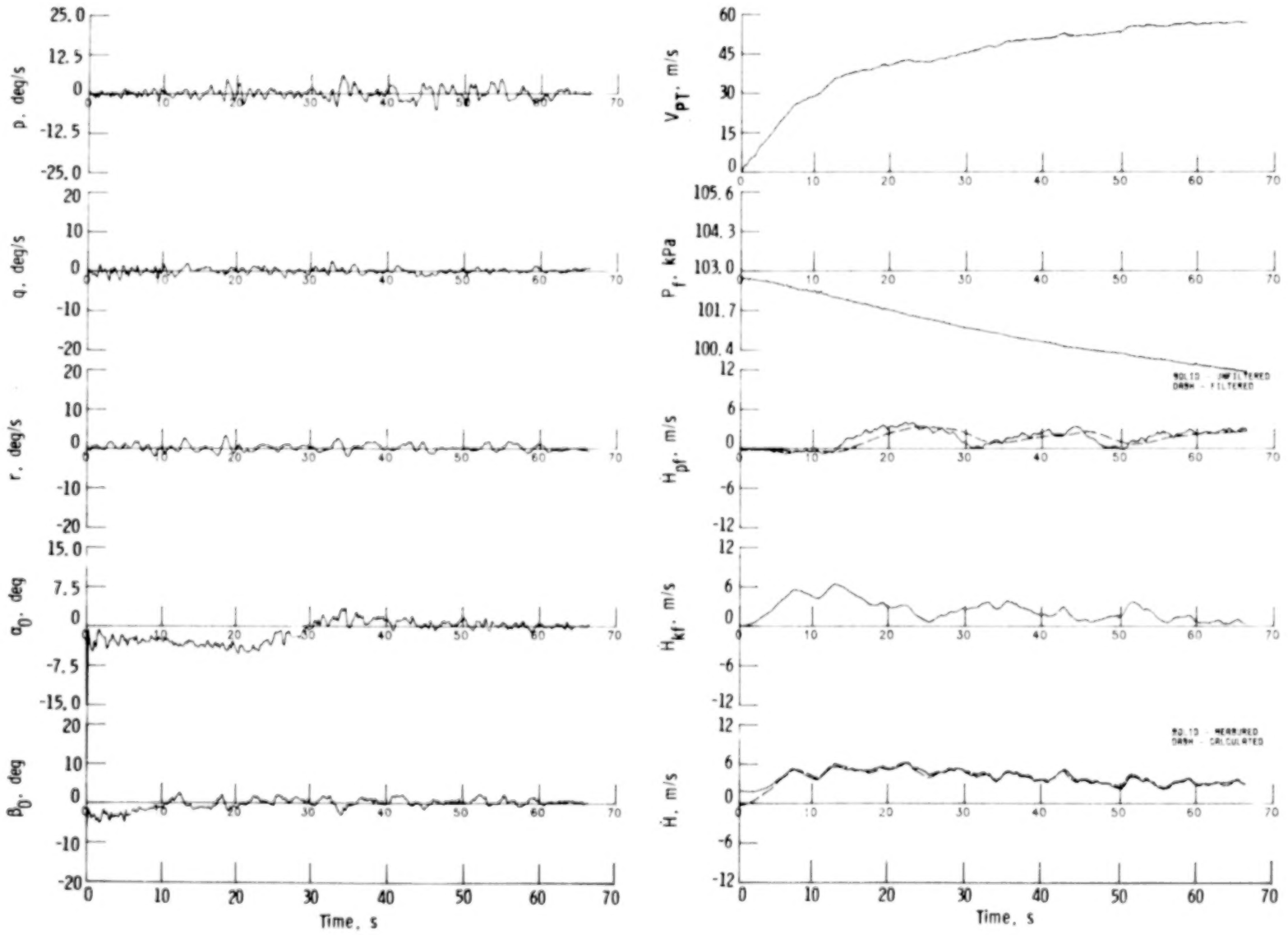

Figure 5.- Take-off; flight 1; run 1.

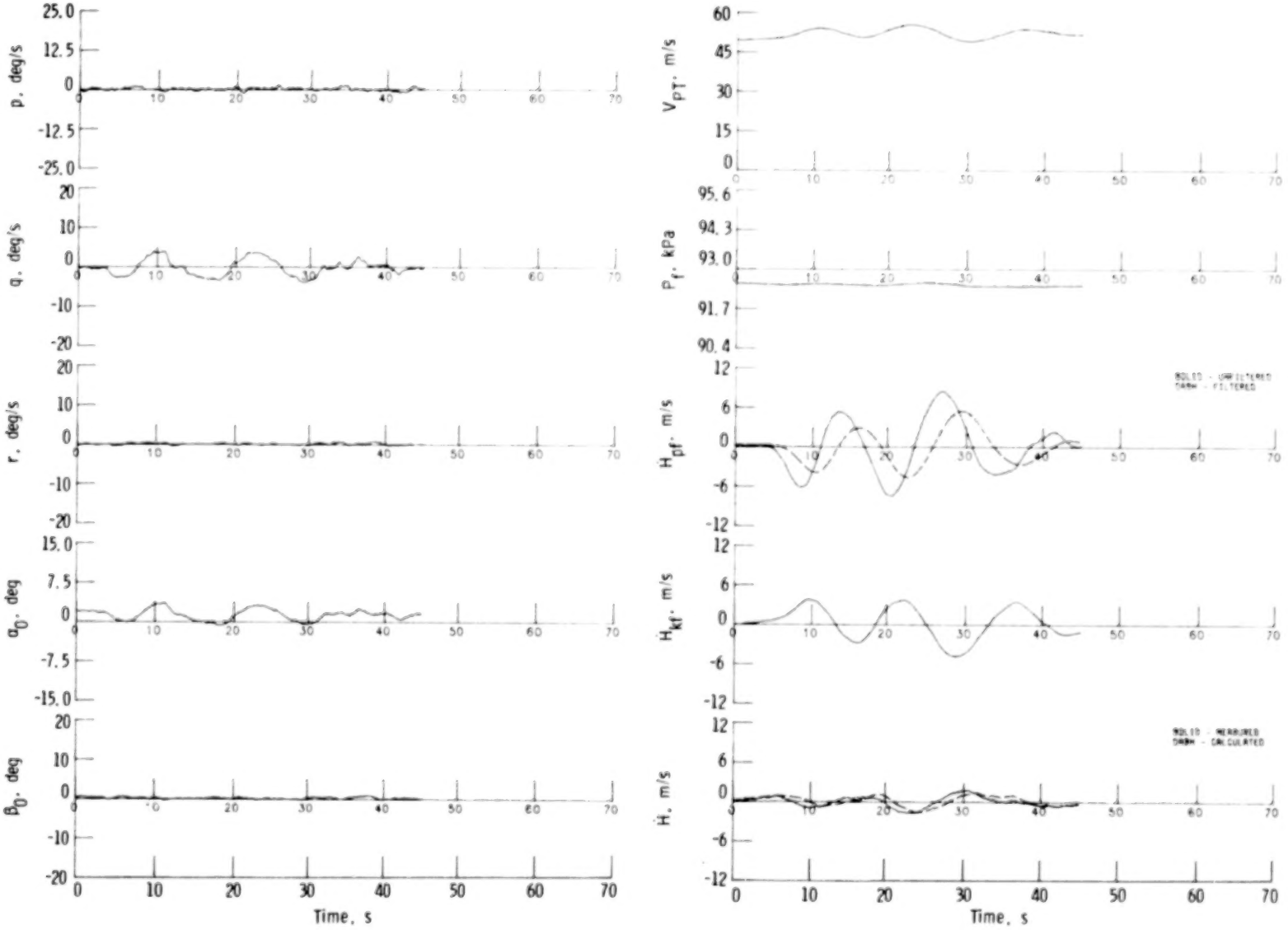

(a) Pitch maneuver.

Figure 6.- Calibration; flight 1; runs 2 and 6.

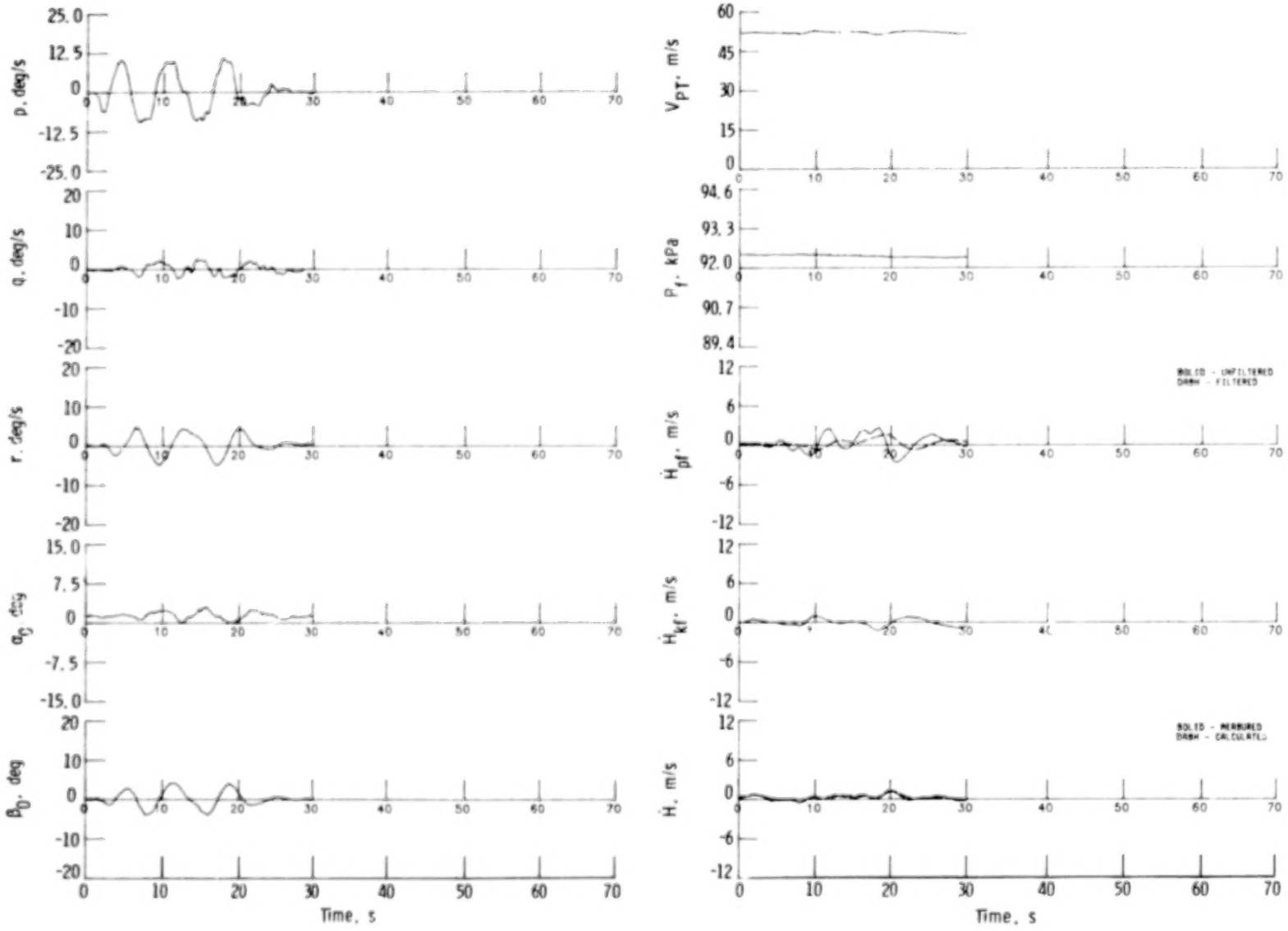

(b) Roll maneuver.

Figure 6.- Continued.

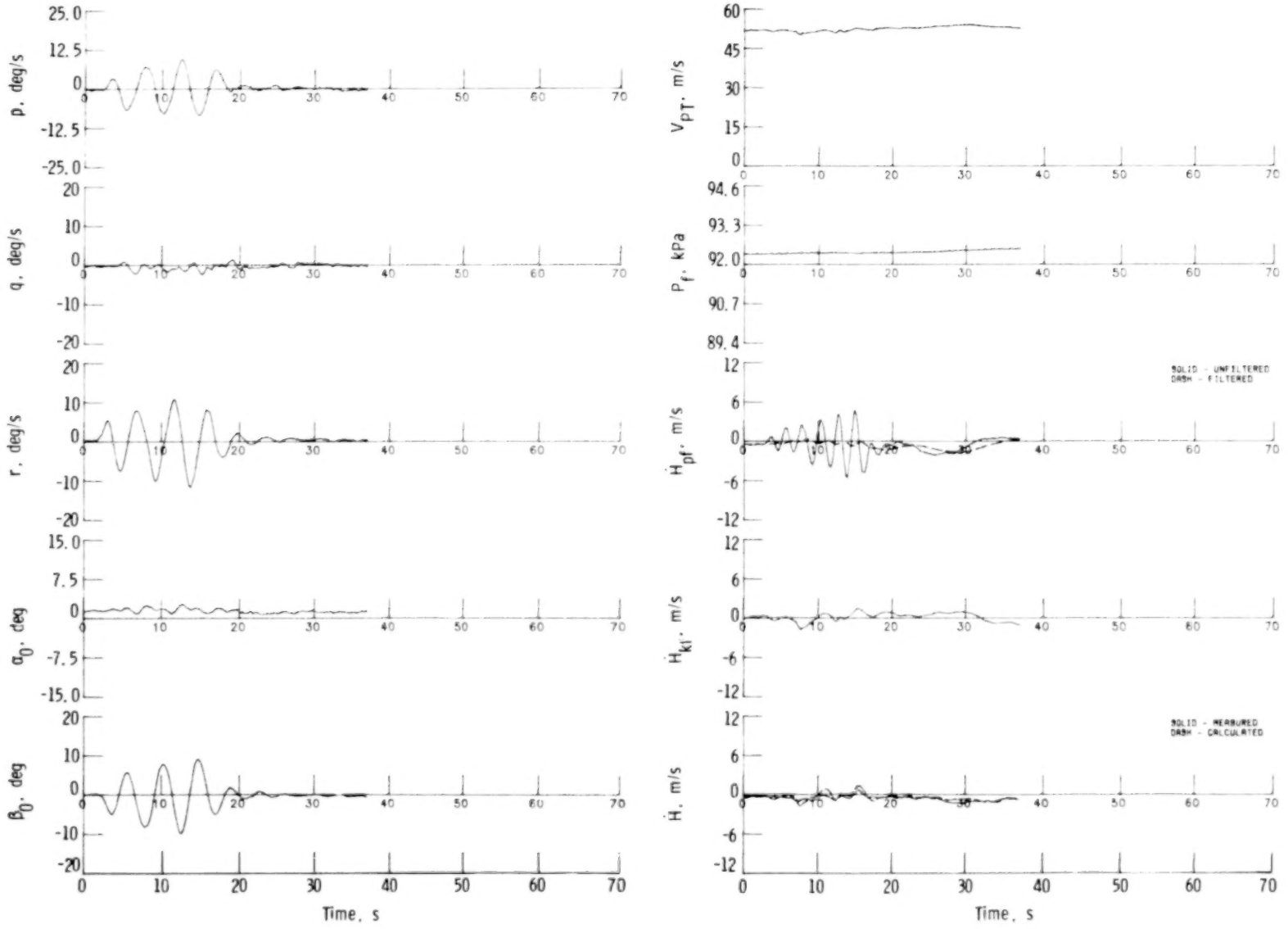

(c) Yaw/roll maneuver.

Figure 6.- Continued.

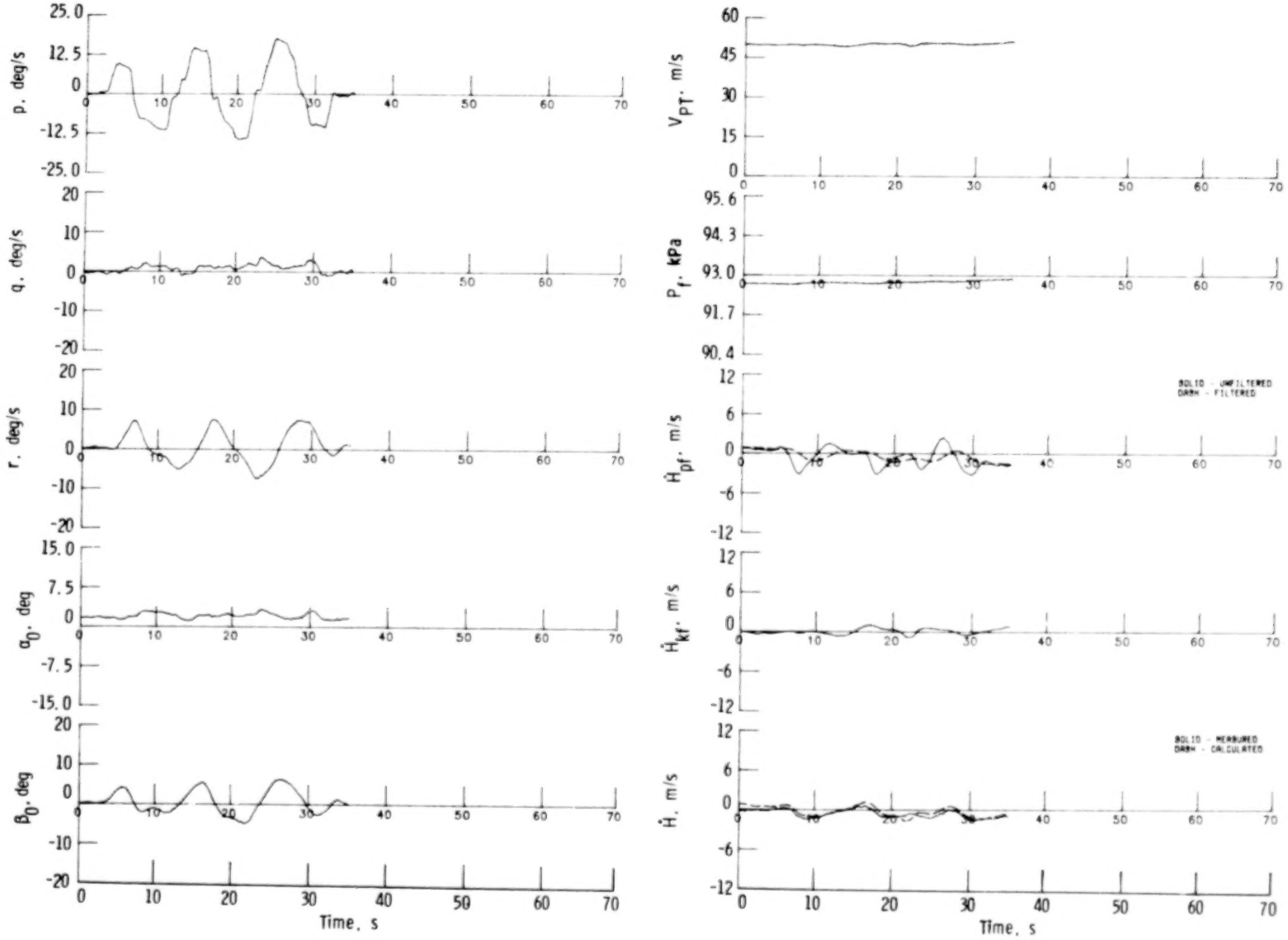

(d) Roll maneuver.

Figure 6.- Concluded.

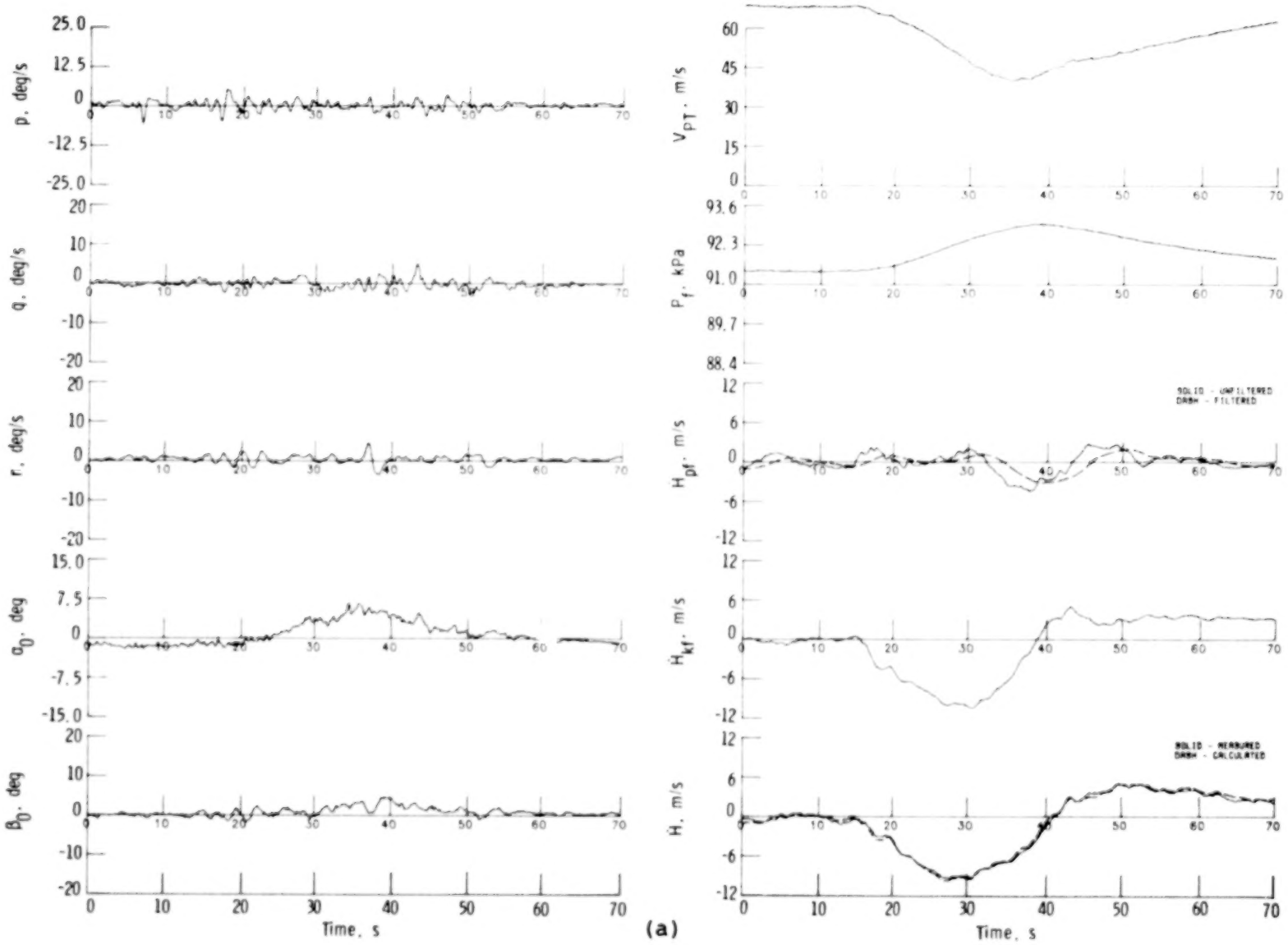

Figure 7.- Kinetic energy change; flight 1; run 3.

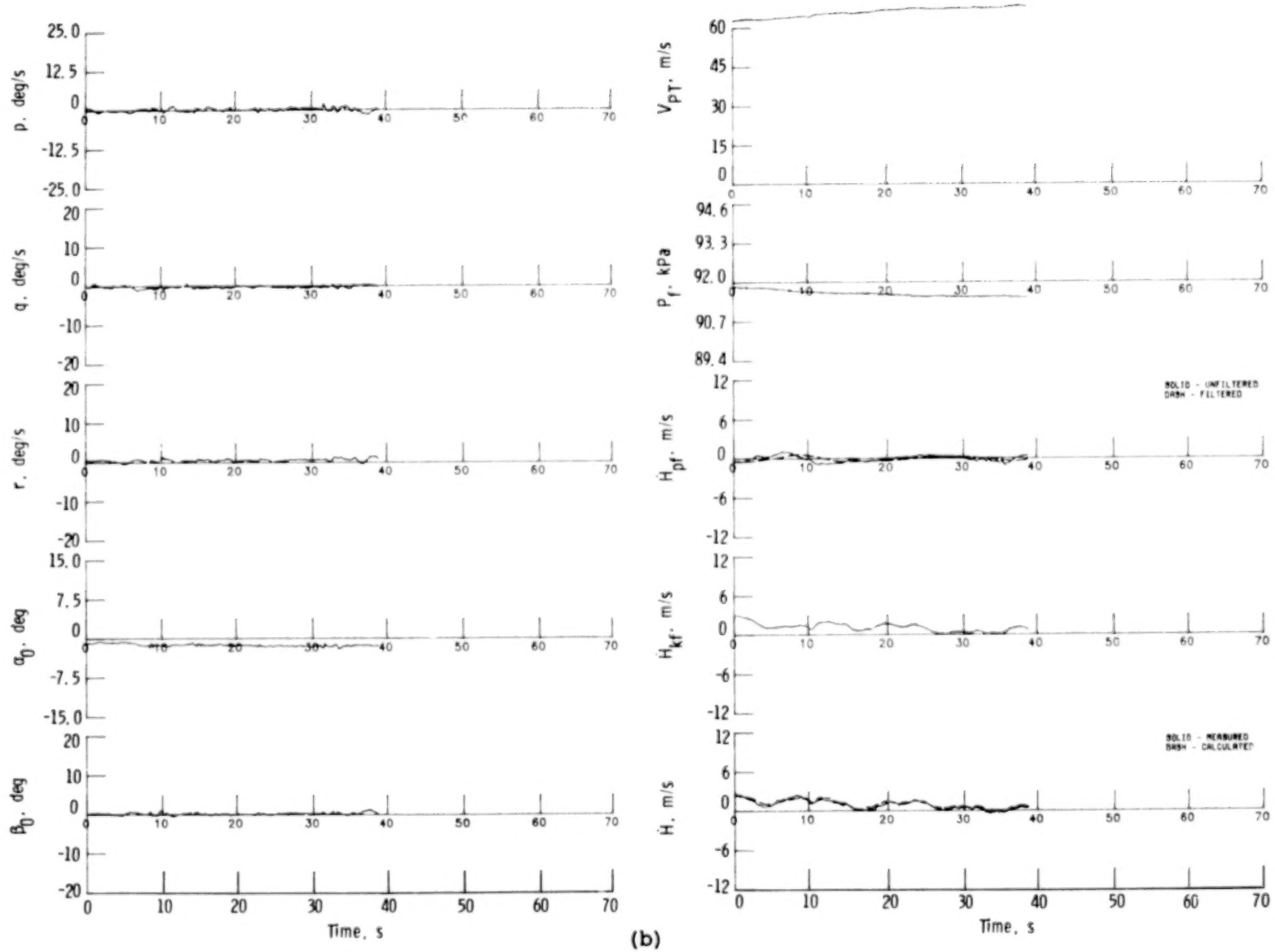

(b)

Figure 7.- Concluded.

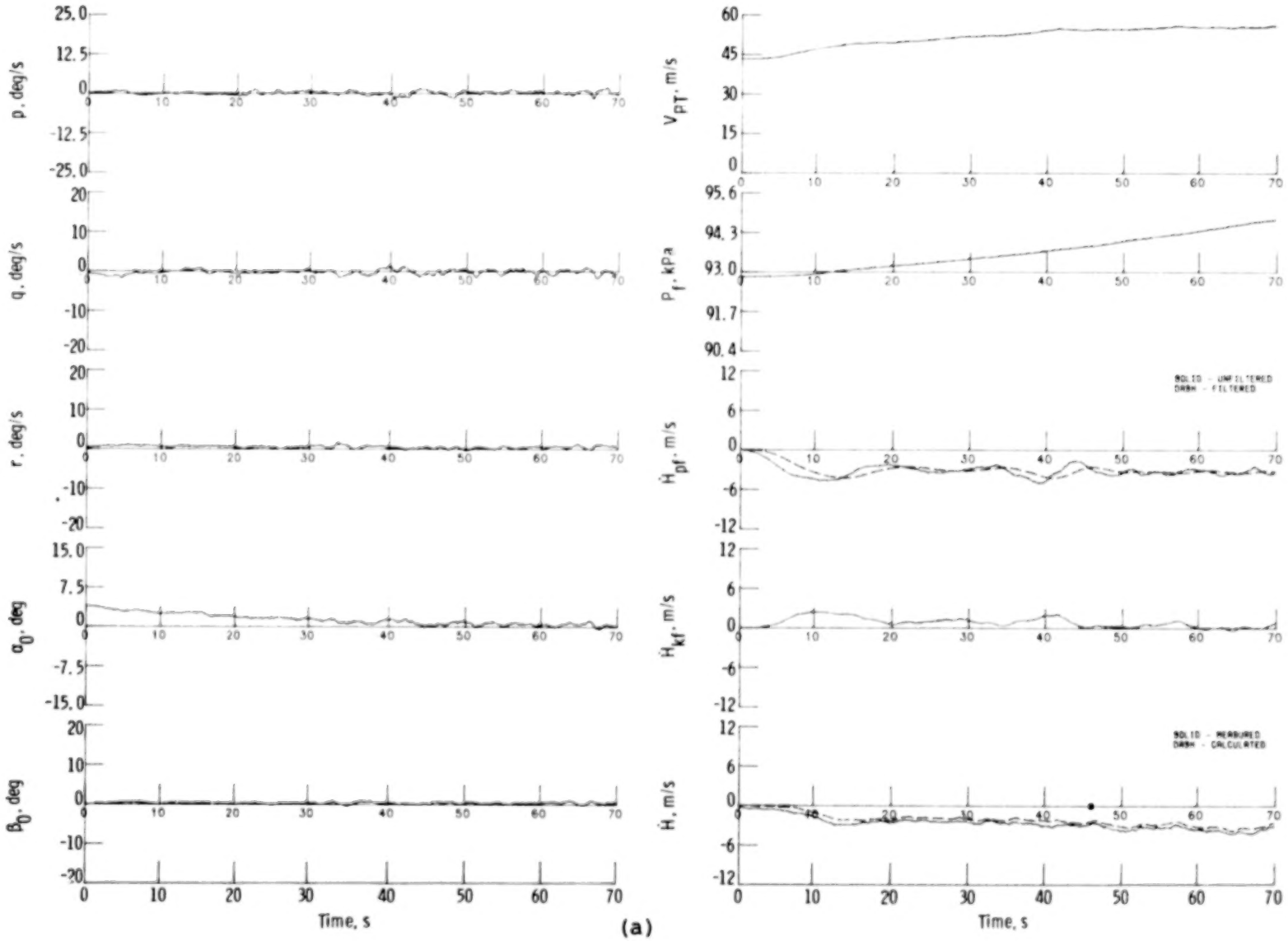

Figure 8.- Potential/kinetic energy exchange; flight 1; run 4.

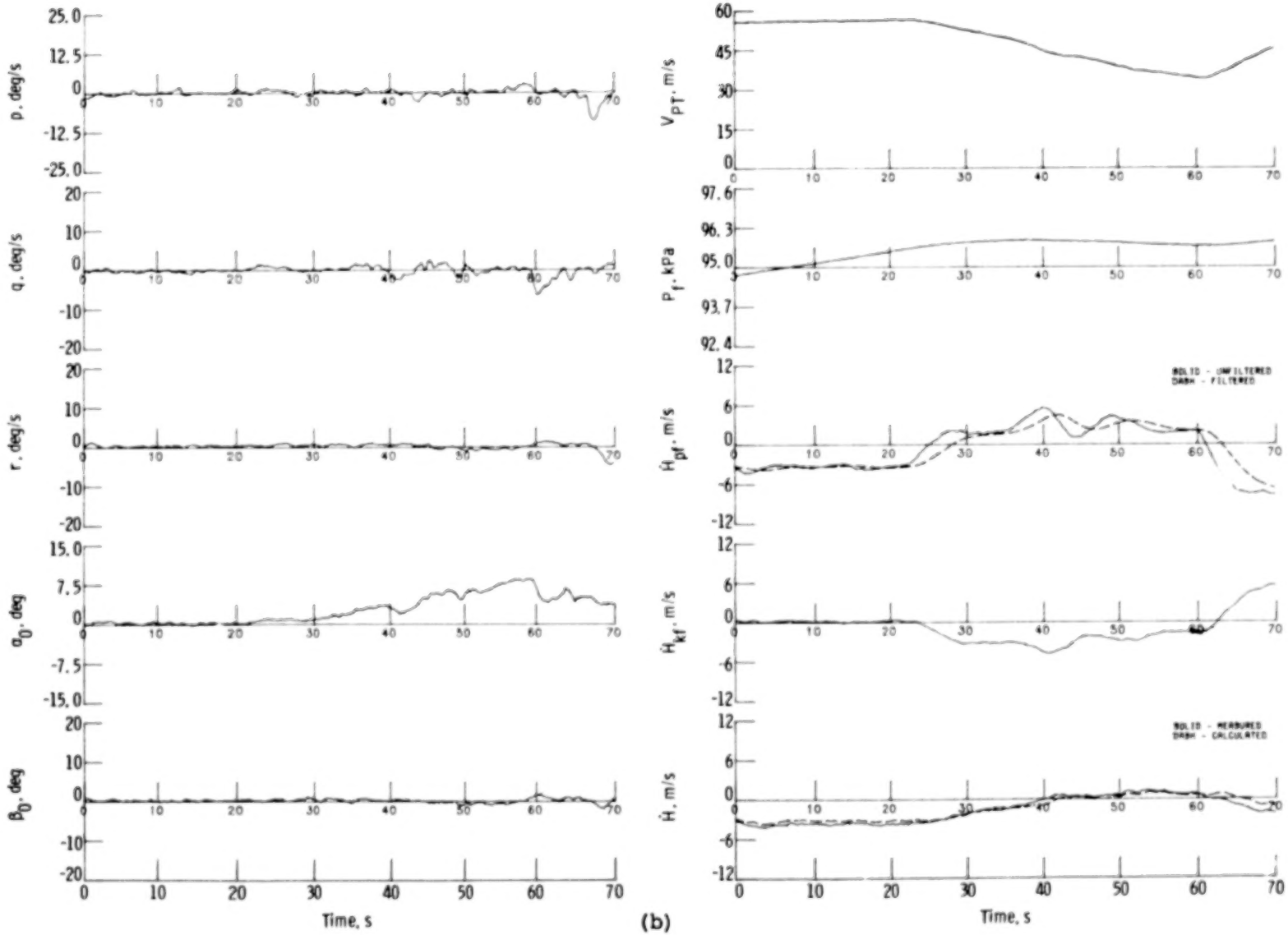

(b)

Figure 8.- Concluded.

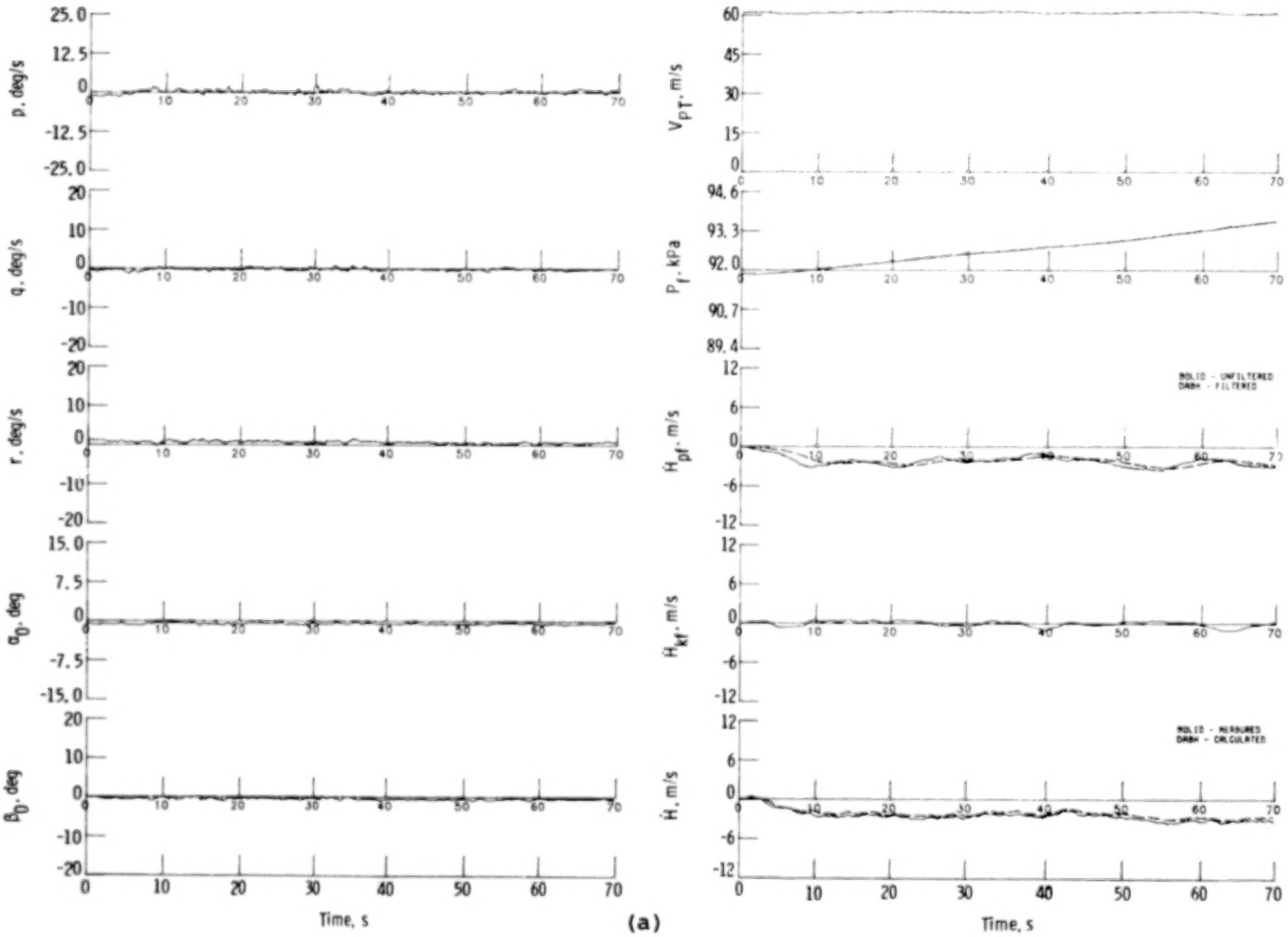

Figure 9.- Potential energy change; flight 1; run 5.

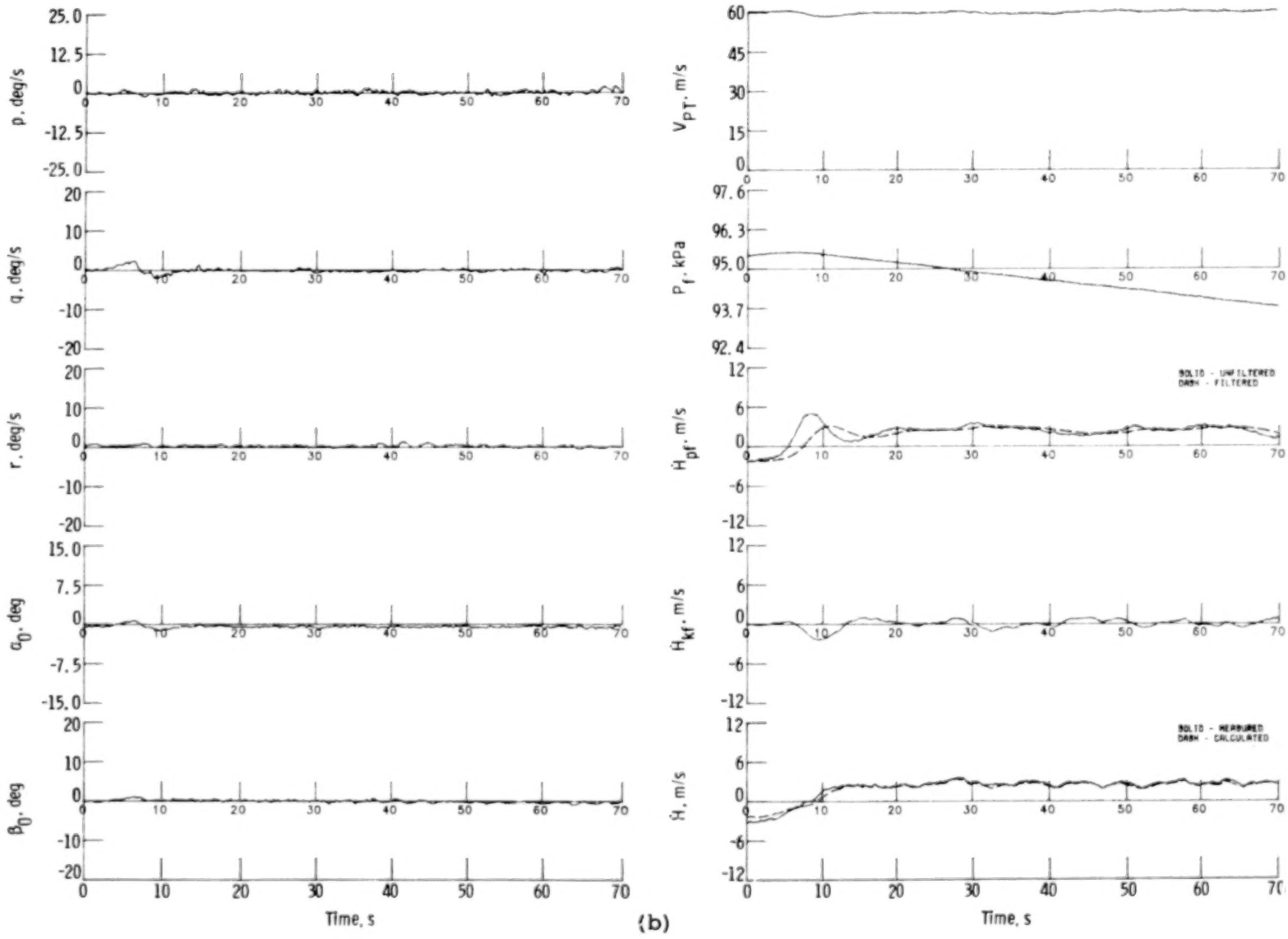

(b)

Figure 9.- Concluded.

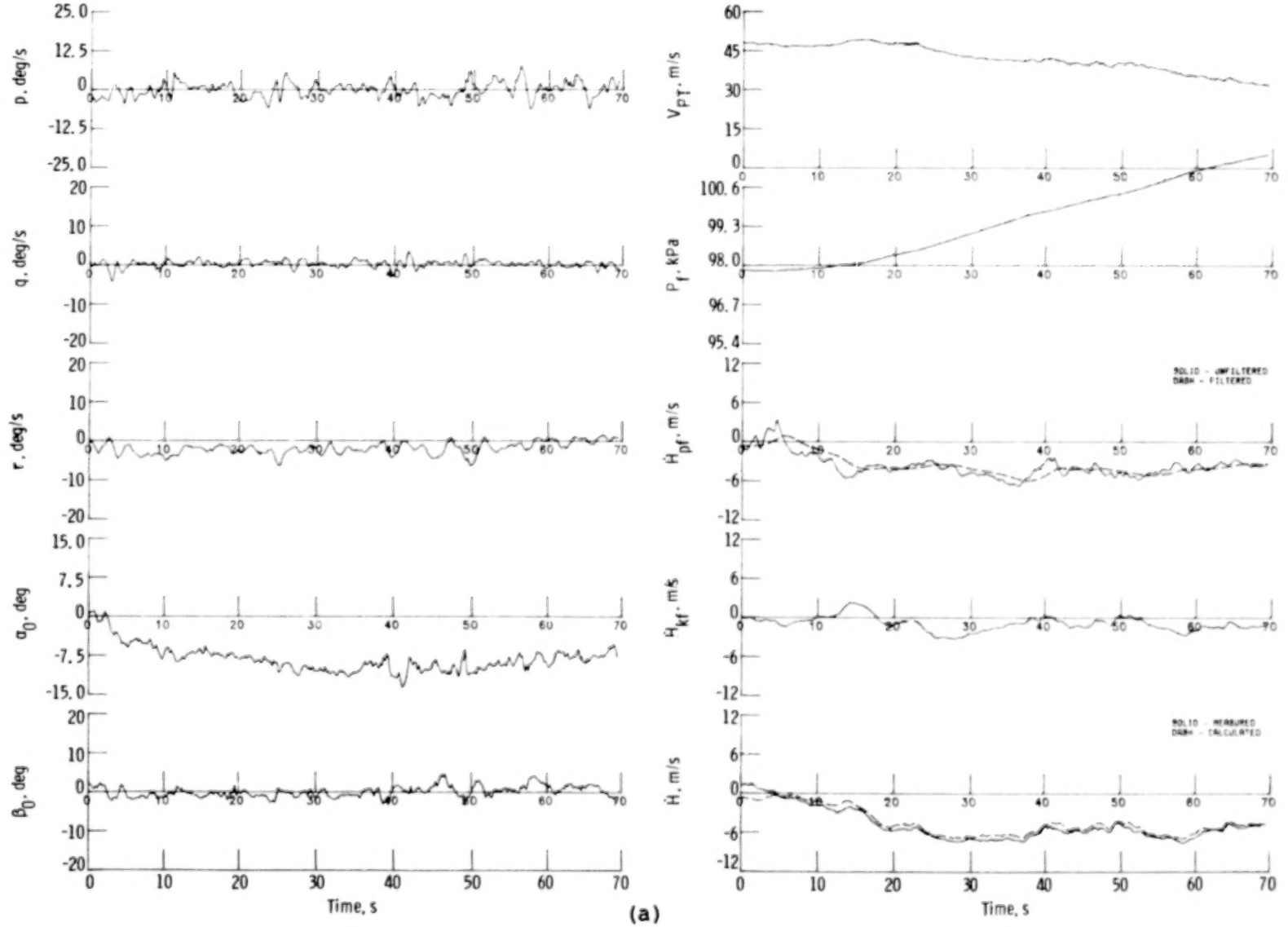

Figure 10.- Landing; flight 1; run 7.

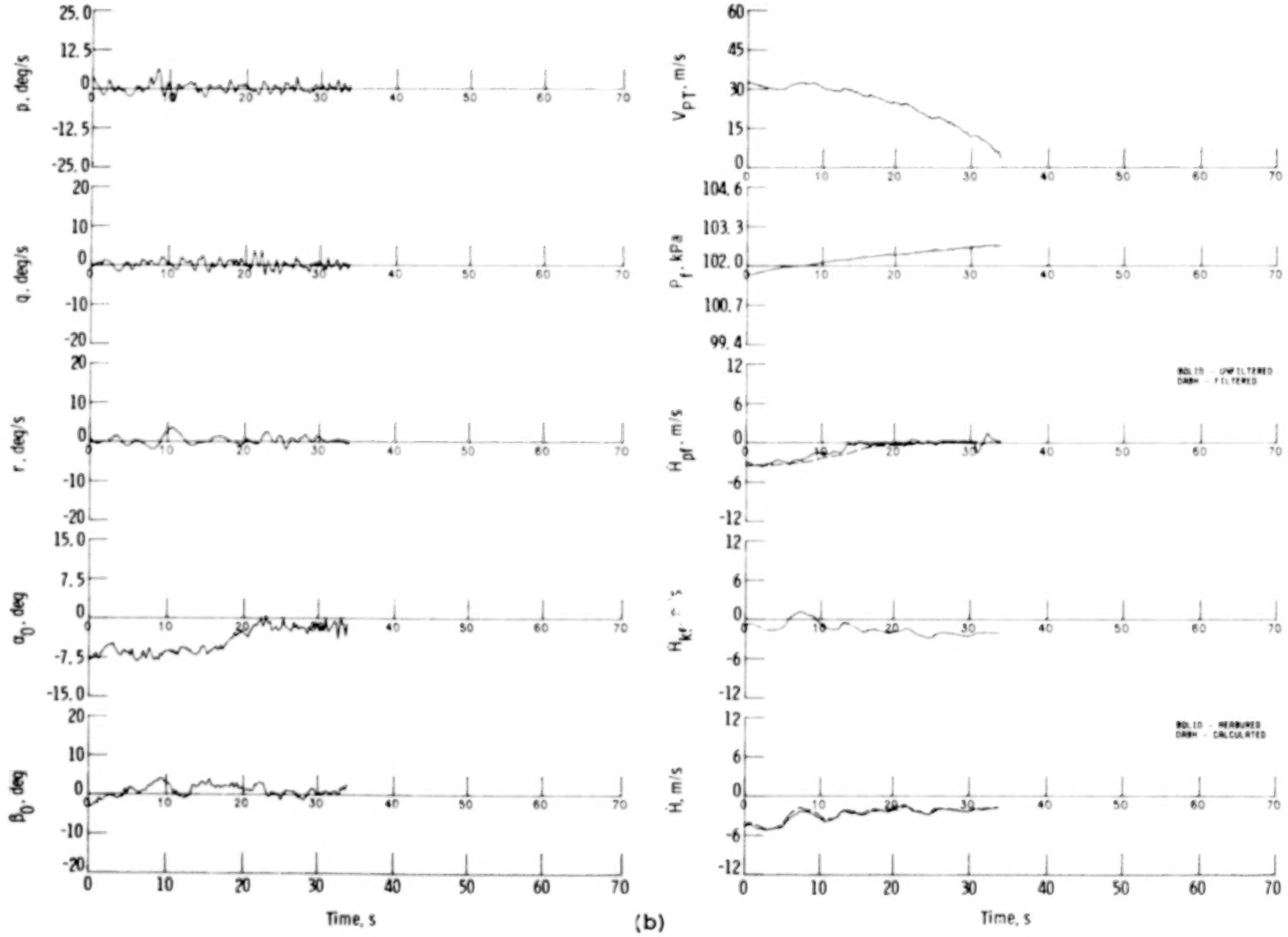

(b)

Figure 10.- Concluded.

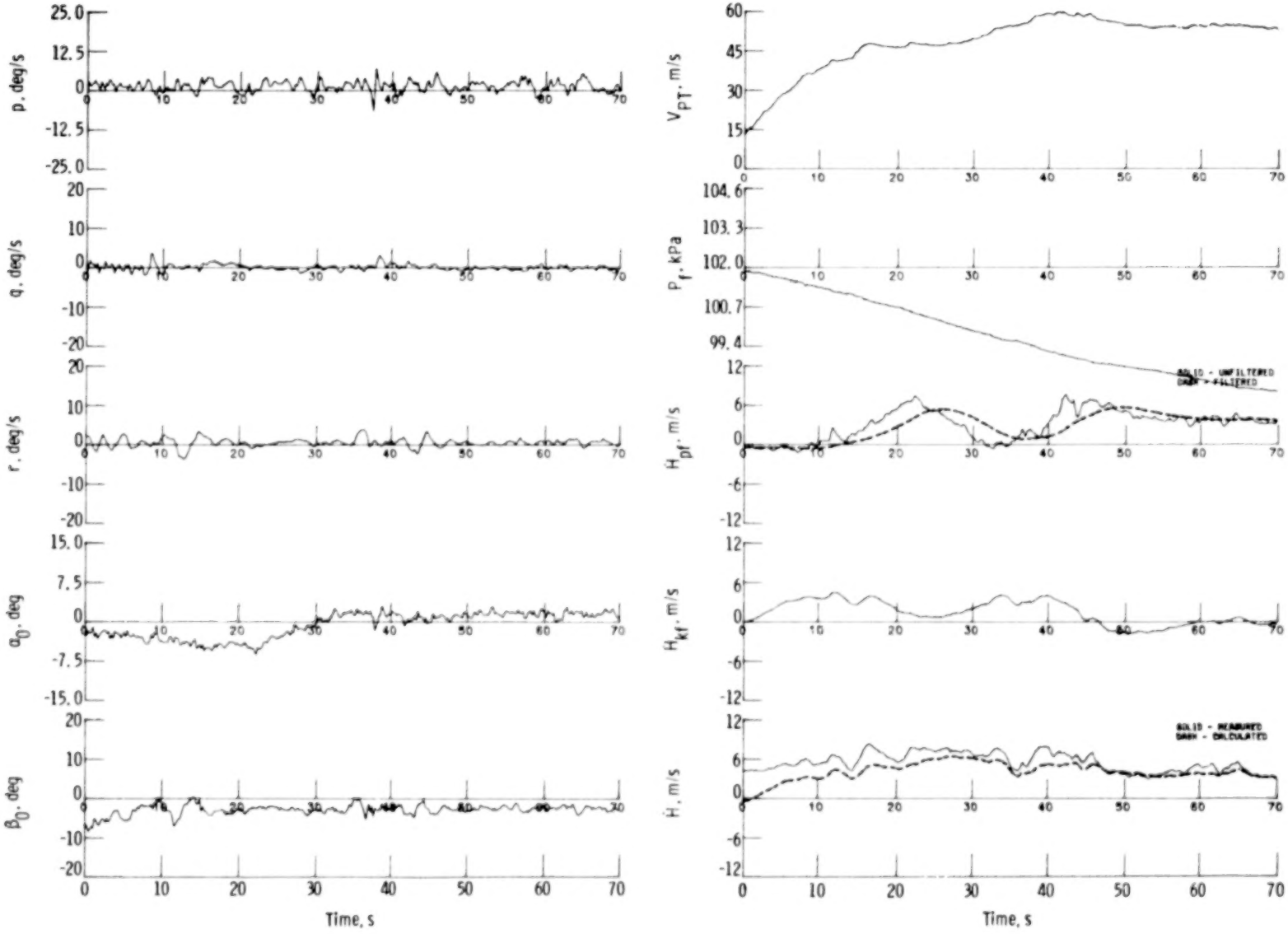

Figure 11.- Take-off; flight 2; run 1.

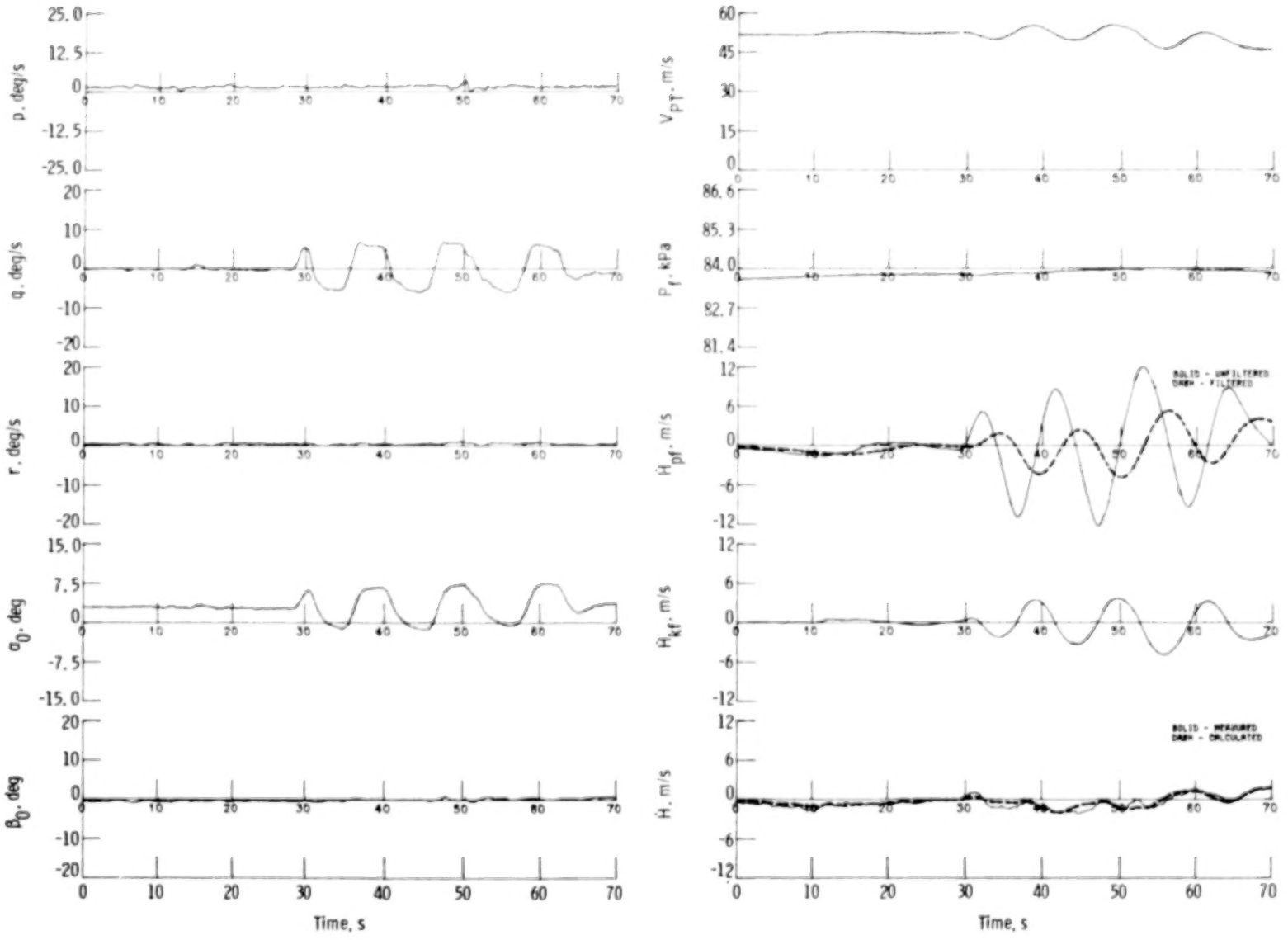

(a) Pitch.

Figure 12.- Calibration maneuvers; flight 2; run 3.

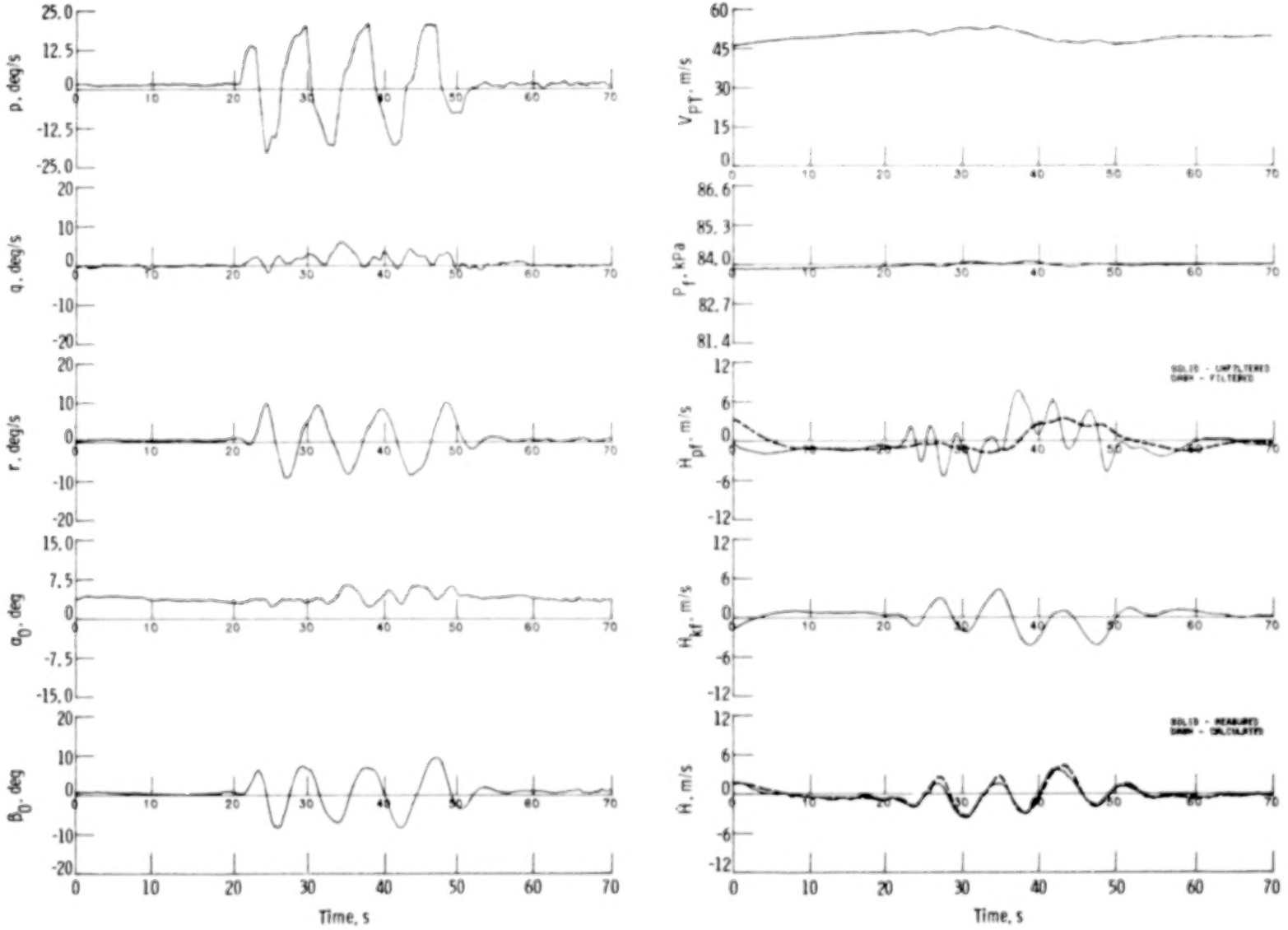

(b) Roll.

Figure 12.- Continued.

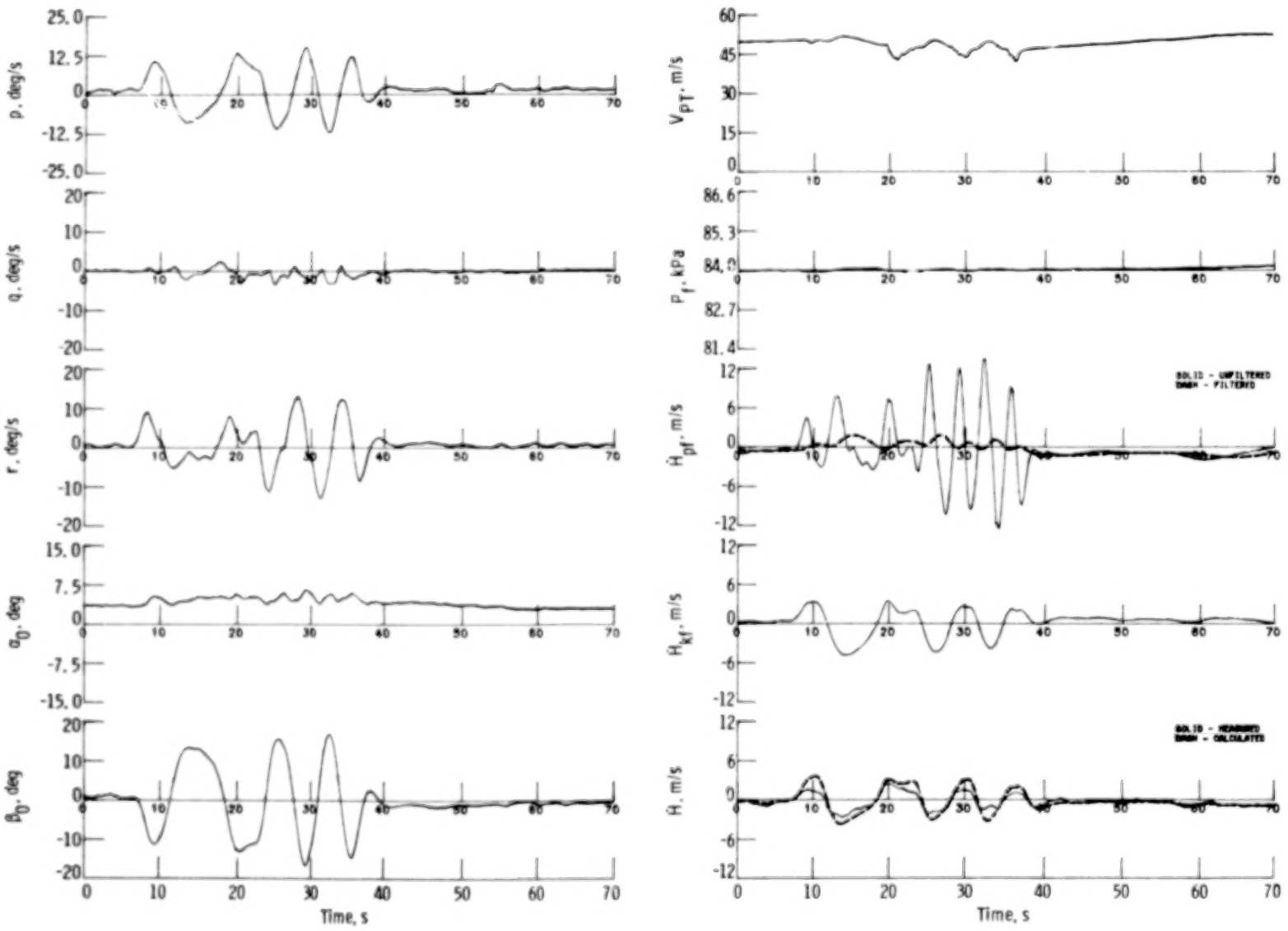

(c) Yaw/roll.

Figure 12.- Continued.

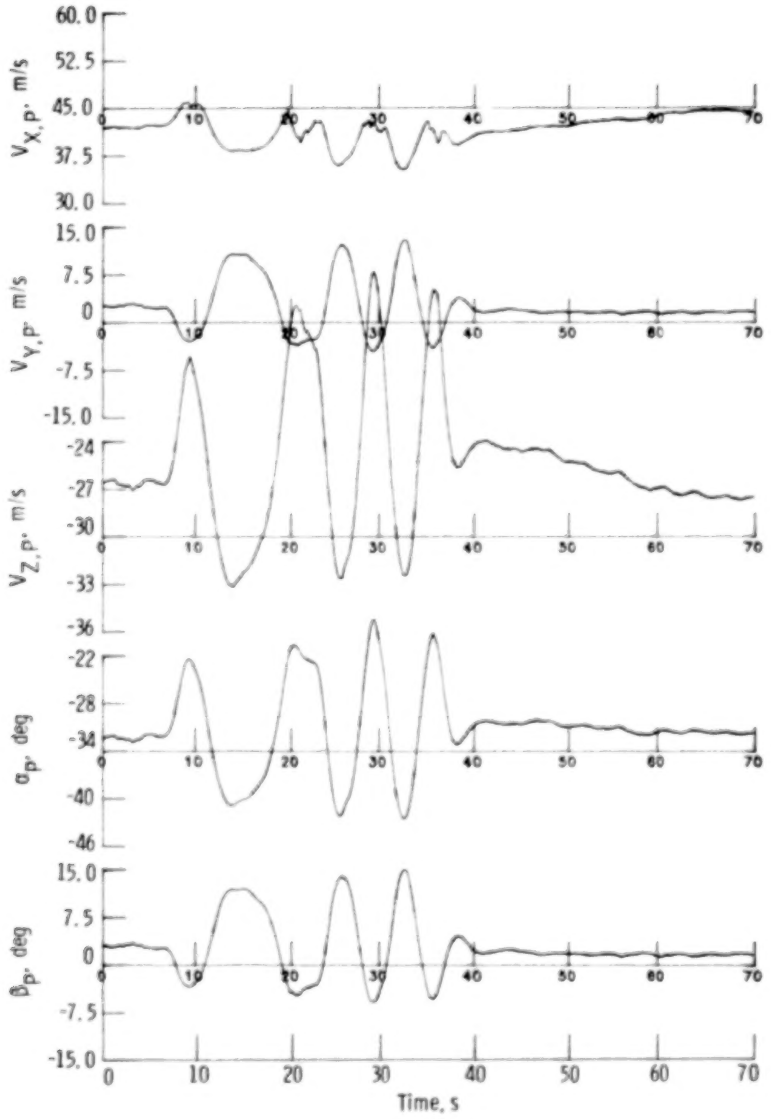

(d) Comparison in probe and coordinate frame.

Figure 12.- Concluded.

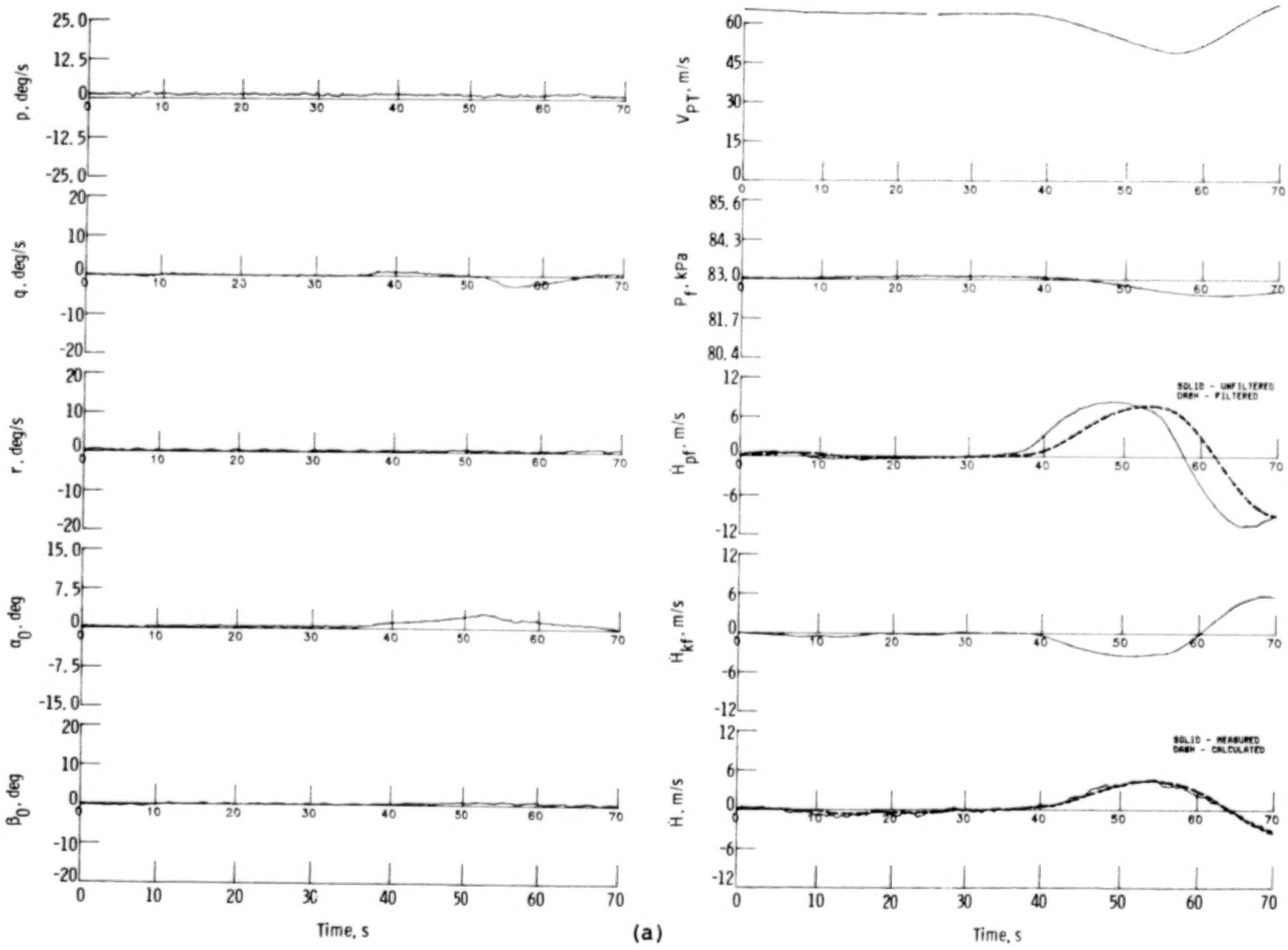

Figure 13.- Potential/kinetic energy exchange; flight 2; run 5.

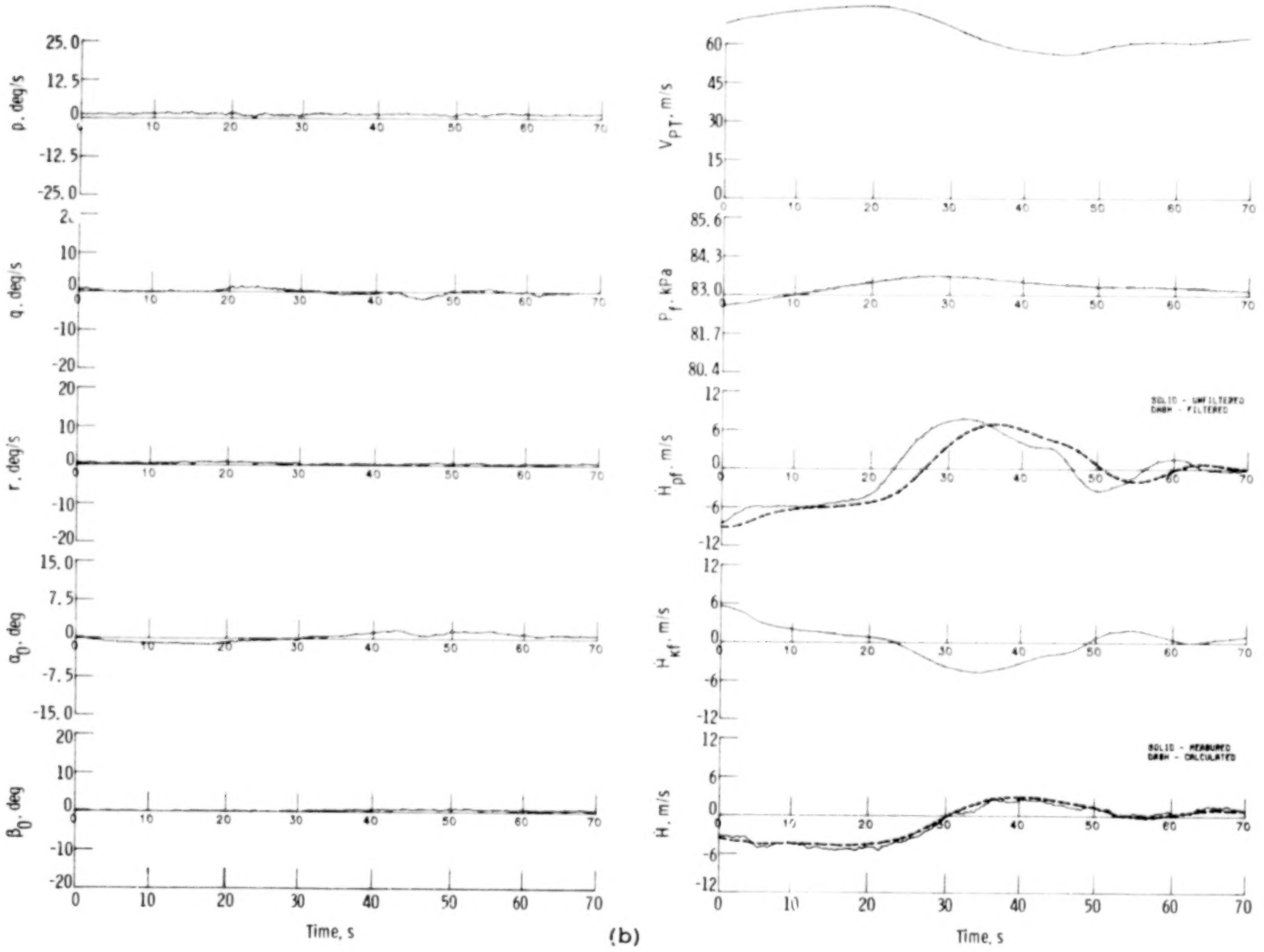

Figure 13.- Concluded.

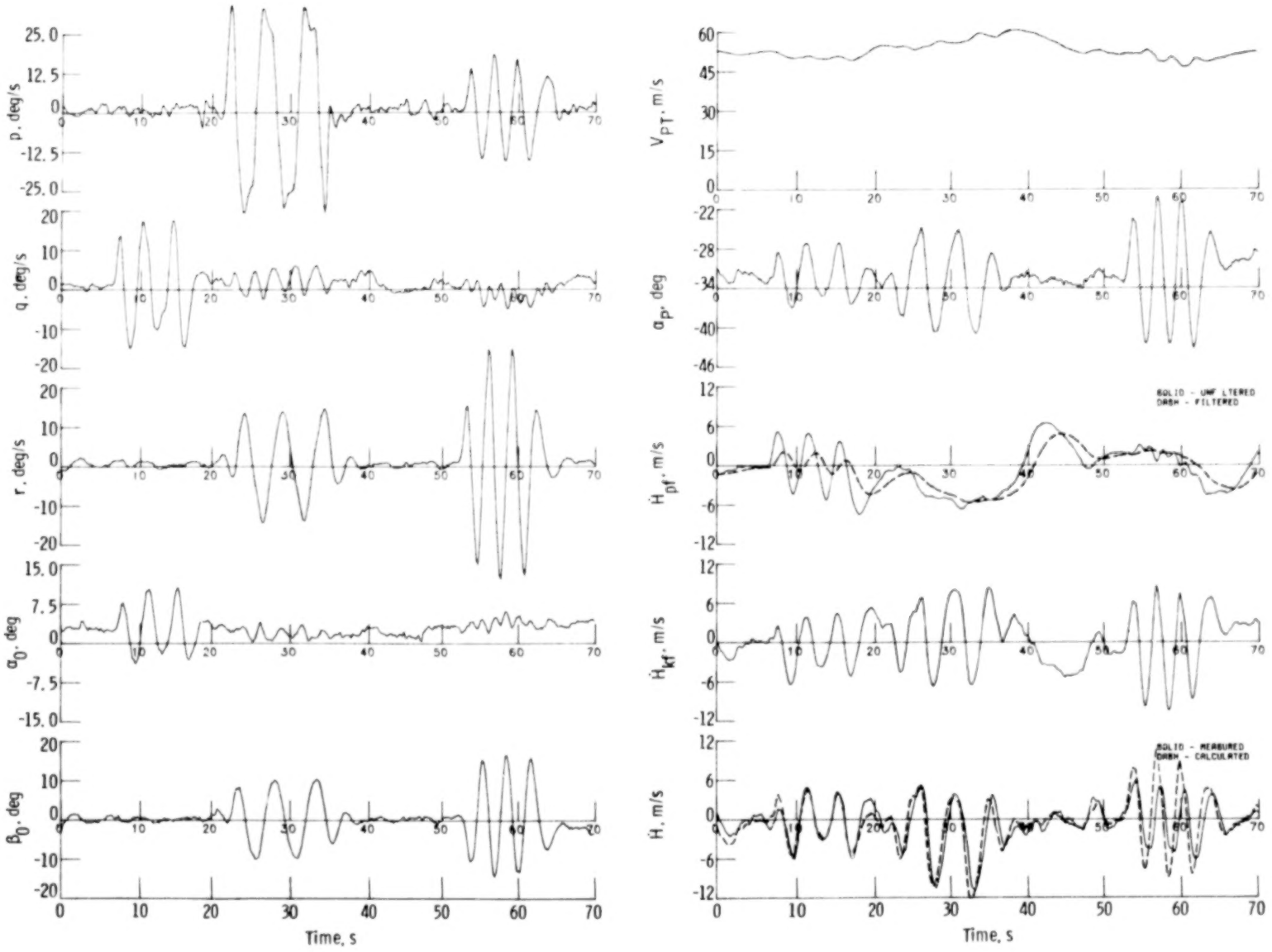

Figure 14.- Calibration maneuvers; flight 3; run 5.

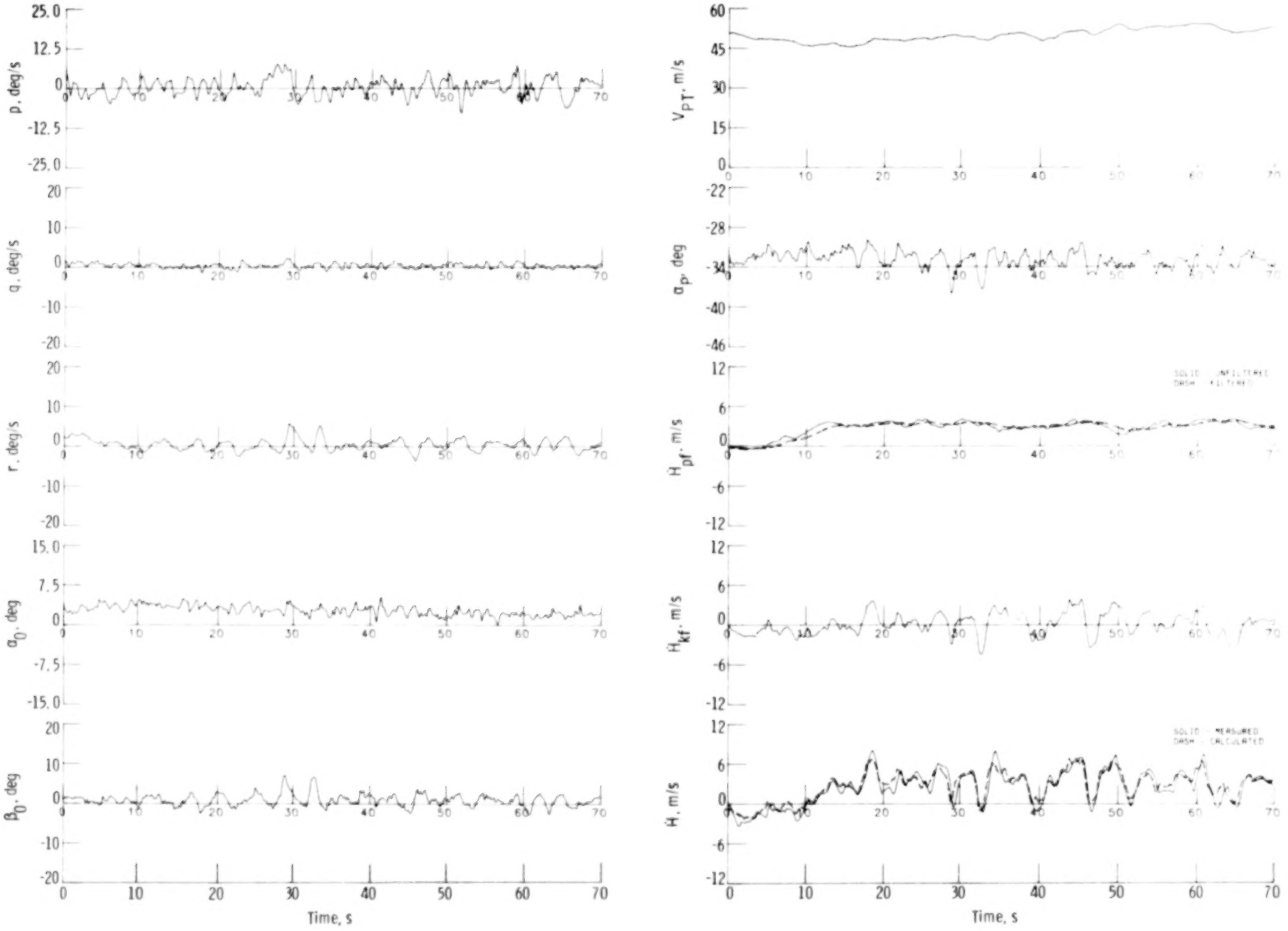

Figure 15.- 3° climb; flight 4; run 14.

1. Report No.	2. Government Accession No.	3. Recipient's Catalog No.
NASA TP-1854		

4. Title and Subtitle	5. Report Date
FLIGHT EVALUATION OF A SIMPLE TOTAL ENERGY-RATE SYSTEM WITH POTENTIAL WIND-SHEAR APPLICATION	May 1981
	6. Performing Organization Code: 505-34-33-01

7. Author(s)	8. Performing Organization Report No.
Aaron J. Ostroff, Richard M. Hueschen, R. F. Hellbaum, and J. F. Creedon	L-14209
	10. Work Unit No.

9. Performing Organization Name and Address	11. Contract or Grant No.
NASA Langley Research Center Hampton, VA 23665	
	13. Type of Report and Period Covered: Technical Paper

12. Sponsoring Agency Name and Address	14. Sponsoring Agency Code
National Aeronautics and Space Administration Washington, DC 20546	

15. Supplementary Notes

16. Abstract

Wind shears can create havoc during aircraft terminal area operations and have been cited as the primary cause of several major aircraft accidents. A simple sensor, potentially having application to the wind-shear problem, has been developed to rapidly measure aircraft total energy relative to the air mass. Combining this sensor with either a variometer or a rate-of-climb indicator provides a total energy-rate system which has been successfully applied in soaring flight. The measured rate of change of aircraft energy can potentially be used on display/control systems of powered aircraft to reduce glide-slope deviations caused by wind shear. This paper describes the experimental flight configuration and evaluations of the energy-rate system. Two mathematical models are developed: the first describes operation of the energy probe in a linear design region and the second model is for the nonlinear region. The calculated total energy rate is compared with measured signals for many different flight tests. Time history plots show the two curves to be almost the same for the linear operating region and very close for the nonlinear region.

17. Key Words (Suggested by Author(s))	18. Distribution Statement
Energy-rate system Wind-shear applications Sensor Aircraft sensor	Unclassified - Unlimited Subject Category 06

19. Security Classif. (of this report)	20. Security Classif. (of this page)	21. No. of Pages	22. Price
Unclassified	Unclassified	49	A03

For sale by the National Technical Information Service, Springfield, Virginia 22161

NASA-Langley, 1981

90%

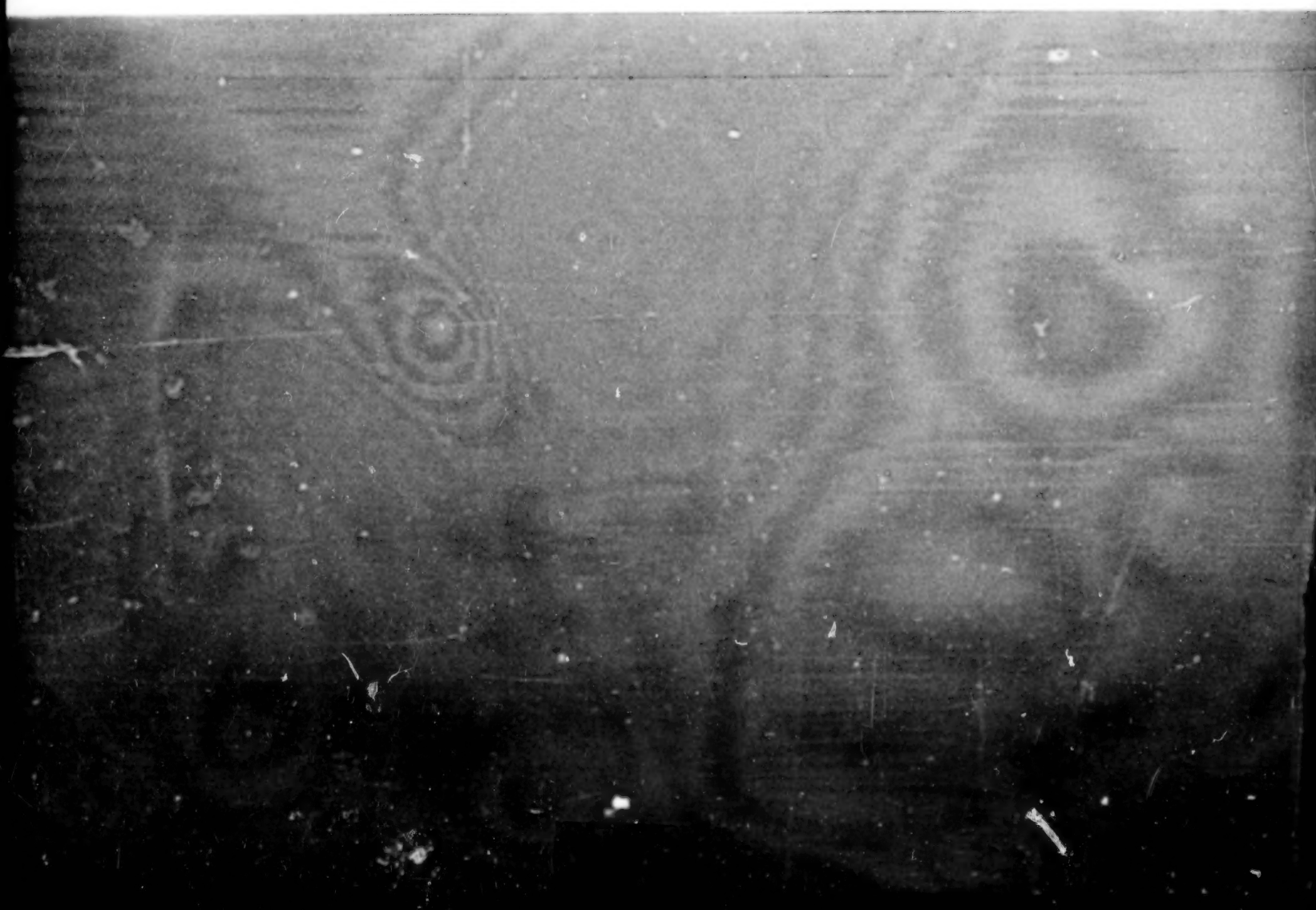

END

10-16-81